

Relativistic Mean Field Approximation to the Analysis of $^{16}O(e, e'p)^{15}N$ data at $|Q^2| \leq 0.4$ (GeV/c) 2

J.M. Udiás¹, J.A. Caballero^{2,3}, E. Moya de Guerra³, Javier R. Vignote¹, A. Escuderos³

¹Departamento de Física Atómica, Molecular y Nuclear, Universidad Complutense de Madrid, E-28040 Madrid, Spain

²Departamento de Física Atómica, Molecular y Nuclear, Universidad de Sevilla, Apdo. 1065, E-41080 Sevilla, Spain

³Instituto de Estructura de la Materia, CSIC Serrano 123, E-28006 Madrid, Spain

Abstract

We use the relativistic distorted wave impulse approximation to analyze data on $^{16}O(e, e'p)^{15}N$ at $|Q^2| \leq 0.4$ (GeV/c) 2 obtained by different groups. Results for differential cross sections, response functions and left-right asymmetry, A_{TL} , are discussed and compared to different sets of experimental data for proton knockout from $p_{1/2}$ and $p_{3/2}$ shells in ^{16}O . We compare with a nonrelativistic approach to identify better the relativistic effects. The present relativistic approach is found to accommodate most of the discrepancy between data from different groups, smoothing a long standing controversy.

PACS: 25.30.Fj; 25.30.Rw; 24.10.-i; 21.60.Cs

Keywords: Quasielastic electron scattering; Negative-energy components; Response functions;; Left-right asymmetry; Relativistic current.

I. INTRODUCTION

Quasielastic $(e, e'p)$ processes are a powerful tool to study bound nucleon properties. Indeed, coincidence $(e, e'p)$ measurements at quasielastic kinematics have provided over the years detailed information on the energies, momentum distributions and spectroscopic factors of bound nucleons. This is so because at quasielastic kinematics the $(e, e'p)$ reaction can be treated with confidence in the impulse approximation, *i.e.*, assuming that the detected knockout proton absorbs the whole momentum (q) and energy (ω) of the exchanged photon (for recent reviews of the subject see ref. [1] and references therein). Until recently most data were concentrated in the low missing momentum range $p_m \leq 300$ MeV/c, where p_m is the recoil momentum of the residual nucleus. In the last years [2] higher p_m -regions are being probed at small missing energies E_m to study further aspects of bound nucleon dynamics and nucleon currents. A substantial amount of theoretical work on $(e, e'p)$ has been carried out on the basis of nonrelativistic approximations to the nucleon current. This is the case of the standard distorted wave impulse approximation (DWIA) [1] that uses a nonrelativistic approximation to the nucleon current operator and wave functions. DWIA has been successfully used over the years [3] to analyze $(e, e'p)$ data using bound and scattered proton wave functions deduced from phenomenological nonrelativistic potentials. However, the standard nonrelativistic DWIA approach have met two major difficulties: a) The spectroscopic factors extracted from analyses of low p_m ($p_m \leq 300$ MeV) data are too small compared with theoretical predictions [4]. As an example, the extracted occupations of $3s_{1/2}$ and $2d_{5/2}$ orbits in ^{208}Pb are $S_\alpha \simeq 0.5$, while theories on short-range correlations [4] predict at most a 30% reduction of mean field occupations for levels just below the Fermi level. b) DWIA calculations compatible with the low- p_m data predict much smaller cross-section in higher- p_m regions (300 MeV $\leq p_m \leq 600$ MeV) than has been experimentally observed [2]. Although short-range correlations are expected to increase the high momentum components, their effect is negligible [5] at the small missing energies of the existing high- p_m data, where effects of long-range correlations have been invoked [2,6].

In the last years we have investigated [7–9] nuclear responses for exclusive quasielastic electron scattering within the framework of relativistic mean field approximations. In the relativistic distorted wave impulse approximation (RDWIA) the one-body nucleon current given by

$$J_N^\mu(\omega, \vec{q}) = \int d\vec{p} \bar{\psi}_F(\vec{p} + \vec{q}) \hat{J}_N^\mu(\omega, \vec{q}) \psi_B(\vec{p}) \quad (1)$$

is calculated with relativistic ψ_B and ψ_F wave functions for initial bound and final outgoing nucleons, respectively. \hat{J}_N^μ is the relativistic nucleon current operator of CC1 or CC2 forms as in [10]. The bound state wave function is a four-spinor with well-defined parity and angular momentum quantum numbers and is obtained by solving the Dirac equation with scalar-vector (S-V) potentials determined through a Hartree procedure from a relativistic Lagrangian with scalar and vector meson terms [11]. The wave function for the outgoing proton is a solution of the Dirac equation containing S-V global optical potentials [12] for a nucleon scattered with asymptotic momentum \vec{p}_F . Dirac equations for both scattered and bound wave functions are solved in coordinate space and their solutions are then transformed to momentum space where necessary. In contrast to DWIA, in RDWIA the analyses

of individual nuclear shells were done with no fitting parameters [13] other than the spectroscopic factors [7,8,14]. The RDWIA spectroscopic factors for the $3s_{1/2}$ and $2d_{3/2}$ shells in ^{208}Pb are larger than the DWIA ones [7,8,14] and are valid for both low- and high- p_m data —values of $S_\alpha \simeq 0.7$ have been obtained [7,14] together with reasonable agreement at high- p_m [9]. Moreover, recent data at high- p_m confirm former predictions of the relativistic approach [15].

When comparing RDWIA to DWIA results, there exist relativistic effects of two kinds, kinematical and dynamical. Kinematical effects are associated to the \vec{p}/M expansions. They can be estimated comparing the Pauli reduction of the current operator [8] to the p/M expansion used in DWIA. For moderate \vec{p}/M values the “relativized” form proposed in [16] gives proper account of such effects. The dynamical effects are linked to the S–V potentials. To this category belongs the effect caused by the nonlocal Darwin term that results in an apparent enhanced absorption when comparing the RDWIA differential cross section to the DWIA one at moderate p_m values, thus predicting larger spectroscopic factors [7]. For larger missing momentum values ($p_m/(Mc) \geq 1/3$) the lower components of the relativistic wave functions start to play a more important role, enhancing the higher momentum components of the nucleon wave functions [9]. Summarizing, RDWIA calculations, compared to standard DWIA, produce lower cross sections at $p_m \leq 300$ MeV/c and larger cross sections at $p_m \geq 300$ MeV/c, thus producing better agreement [7–9] with experiment.

We have recently studied [15,17,18] the effect of the relativistic treatment of the nucleon current on the individual response functions. Studies within the relativistic plane wave impulse approximation (RPWIA), where the interaction between the ejected nucleon and the residual nucleus (FSI) is neglected, showed that the interference transverse–longitudinal response (TL) is very sensitive to the negative-energy components of the relativistic bound nucleon wave function. We have also shown [18] that for the $j = \ell \pm 1/2$ spin-orbit partners of a given shell, this sensitivity is much larger for the $j = \ell - 1/2$ (jack-knifed) than for the $j = \ell + 1/2$ (stretched) case. These are dynamical relativistic effects that have been also clearly observed in a more realistic description of the $(e, e'p)$ reaction including relativistic FSI [15]. In ref. [19] our relativistic calculations for differential cross section, TL response function (R^{TL}), and left-right asymmetry (A_{TL}) were compared to the experimental data measured at $|Q^2| = 0.8$ (GeV/c) 2 . The good agreement found proves the crucial role played by both kinematical and dynamical relativistic effects. In particular, the richness shown by the structure of the left-right asymmetry is only consistent with predictions of relativistic calculations that include the dynamic enhancement of the lower components of Dirac spinors.

So far, the relativistic model has been applied successfully at low $|Q^2|$ in ^{40}Ca and ^{208}Pb [7,9] and at high $|Q^2|$ in ^{16}O [15,19]. For this last nucleus, there is an important controversy in the theoretical comparisons to the data measured at $|Q^2|$ values below 0.4 (GeV/c) 2 . Indeed, 1p-shell proton knockout experiments on ^{16}O have been performed at Saclay [20] and NIKHEF [21,22] in various kinematics. These experiments measured the cross section as a function of missing momentum and, in particular, Chinitz *et al.* [20] and Spaltro *et al.* [21] extracted also the TL response and left-right asymmetry, A_{TL} , at $|Q^2| = 0.3$ (GeV/c) 2 and 0.2 (GeV/c) 2 , respectively. The measurements from Chinitz *et al.* [20] were compared to relativistic DWIA calculations and showed relatively small deviations with respect to the theory. On the other hand, in ref. [21] a comparison was made to results from standard nonrelativistic DWIA calculations, that were found to be far from data. For

instance, using standard nonrelativistic DWIA calculations with optical potential parameters by Schwandt *et al.* [23] and spectroscopic factors that give a proper account of data taken in parallel kinematics, Spaltro *et al.* [21] found that the experimental R^{TL} is enhanced by a factor $\simeq 2.05$ for the $1p_{3/2}$ shell and by a factor $\simeq 1.5$ for the $1p_{1/2}$. On the contrary, the data taken at Saclay [20] are much closer to the theoretical calculations, both relativistic and nonrelativistic.

Some authors [6,24] have explained the large discrepancy found by Spaltro *et al.* within nonrelativistic DWIA by invoking two-body currents. However, the results in [6] are not consistent with other studies of two body currents in exclusive electron scattering reactions [25]. Hence, the controversy surrounding the TL response and asymmetry data still persists. Here we try to straighten this question up. As above stated, in many previous analyses of the low Q^2 data on ^{16}O , including or not two-body currents, the theoretical calculations were based on standard nonrelativistic DWIA, with the exception of the theoretical curves presented in ref. [20]. Motivated by the success of relativistic descriptions of electron scattering observables above described, as well as of normal polarization observables in ^{12}C at $|Q^2| \simeq 0.5$ (GeV/c) 2 [26], we investigate here whether a systematic fully relativistic analysis of the $(e, e'p)$ data at low $|Q^2|$ may explain the apparent discrepancies between sets of data from Saclay [20] and NIKHEF [21,22].

Kinematical conditions of these experiments allow us to assume that processes like multi nucleon emission, baryonic excitations or meson production play no role and consequently the reaction mechanism is mainly governed by the one-body current (impulse approximation). Sensitivity of the various scattering observables (cross sections, responses and asymmetries) to the dynamical and kinematical relativistic effects is discussed.

The paper is organized as follows: in Section II we summarize the basic formalism needed to describe coincidence electron scattering reactions, paying special attention to the relativistic distorted wave impulse approximation (RDWIA). Section III contains the theoretical results obtained and their comparison with the experimental data. In section IV we present our conclusions.

II. FORMALISM FOR $(E, E'P)$ REACTIONS

The general formalism for exclusive electron scattering reactions has been presented in detail in several previous papers. We refer in particular to refs. [1,7,27]. Here we just summarize the kinematics and focus on those aspects that are of relevance to the points under discussion in this paper. As a guide to the reader we write down the unpolarized cross section in Born approximation assuming plane waves for the incoming and outgoing electron (treated in the extreme relativistic limit),

$$\frac{d\sigma}{d\Omega_e d\varepsilon' d\Omega_F} = K \sigma_{Mott} f_{rec} \left[v_L R^L + v_T R^T + v_{TL} R^{TL} \cos \phi_F + v_{TT} R^{TT} \cos 2\phi_F \right] \quad (2)$$

where ε' and Ω_e are the energy and solid angle corresponding to the scattered electron and $\Omega_F = (\theta_F, \phi_F)$ is the solid angle for the outgoing proton. The factor K is given by $K = |\vec{p}_F| E_F / (2\pi)^3$, with \vec{p}_F the momentum carried by the ejected proton and E_F its energy. The term f_{rec} is the usual recoil factor $f_{rec}^{-1} = |1 - (E_F/E_{A-1})(\vec{p}_{A-1} \cdot \vec{p}_F)| / |\vec{p}_F|^2$, where \vec{p}_{A-1} and E_{A-1} are the momentum and energy of the residual nucleus, respectively. The kinematical

factors are $V_L = \lambda^2$, $V_T = \lambda/2 + \tan^2 \theta_e/2$, $V_{TT} = \lambda/2$, $V_{TL} = \lambda\sqrt{\lambda + \tan^2 \theta_e/2}$ with $\lambda = 1 - (\omega/|\vec{q}|)^2$, where ω and \vec{q} are the energy and momentum transfer in the reaction and θ_e the electron scattering angle. These factors that contain the dependence on the electron kinematics coincide with those given in [27,28] except for a factor $\sqrt{2}$ in the interference TL term. We remark that in refs. [20,21] a different convention for K was used (see for instance eq. (1) of ref. [21]). This amounts to a factor M/E_F of the responses presented in this work with respect to the ones displayed in refs. [20,21]. Our calculation of differential cross-sections and responses includes also the effect of Coulomb distortion of the incoming and outgoing electron waves. This breaks the simplicity of eq. (2), which is however still useful as a guide. The response R^{TL} is obtained from differential cross-sections at $\phi_F = 0^\circ$ and 180° , as in experiment. Nevertheless, for ^{16}O Coulomb distortion effects in the electron wave functions are tiny (less than 1.5% in the cross-section).

The hadronic current enters only in the response functions R^α , $\alpha = L, T, TL, TT$ where L and T denote the longitudinal and transverse projections of the nuclear current with respect to the momentum transfer \vec{q} , respectively. Note that the response functions can be separated by performing measurements with different kinematical factors v_α and/or values of the azimuthal angle ϕ_F , while keeping the momentum and energy transfer constant. A theoretical evaluation of the response functions requires knowledge of the four-vector nuclear current operator.

Quite often, experimental data for the cross-section are presented in terms of *reduced cross-sections* or *effective momentum distributions* $\rho(\vec{p}_m)$, obtained by integrating over a particular missing energy peak the differential cross-section divided by $K\sigma_{ep}$. Thus $\rho(\vec{p}_m)$ is defined by,

$$\rho(\vec{p}_m) = \int_{\Delta E_m} \left(\frac{d\sigma}{d\Omega_e d\varepsilon' d\Omega_F dE_F} / (K\sigma_{ep}) \right) dE_m. \quad (3)$$

The free electron-proton cross section, σ_{ep} , is usually taken as σ_{CC1} of de Forest [10]. One must be aware that the cross-section given in eq. (2) has a strong dependence in the kinematical variables via K and σ_{ep} . For instance, at the kinematics of the experiment of Chinitz *et al.* [20] ($T_F = 160$ MeV, $|Q^2| = 0.3$ (MeV/c) 2 and $\varepsilon_{beam} = 580$ MeV) a small variation of 5 MeV in T_F and ω , keeping E_m and p_m constant, may change the cross-section by as much as 7%. Most of this kinematics and phase-space dependence is removed in the reduced cross-section and in the nuclear responses, which thus depend much less on kinematics. Their corresponding variation is less than 2% for the above example of 5 MeV change in T_F and ω . Experimentally, a folding and average over the experimental acceptance of the cross-sections, responses, or reduced cross-sections is performed, and one or several central values for the kinematical variables are quoted so that the theoretical calculations can be done for these central variables. Due to this, it is not unusual that the spectroscopic factor, that is, the scale factor between the theoretical calculation and the data, may depend on whether one chooses to set the scale by comparing to reduced cross-sections or to differential cross-sections, or even to separate responses. In principle, the scale factor should be set after minimizing kinematical dependences. To do so, in this work we derive the spectroscopic factor (S_α) from the reduced cross-section data. Then we use this same factor for the individual responses. In this way the analyses of R^{TL} and other data on nuclear responses are more consistent and meaningful.

Another quantity also obtained by the experimentalists is the left-right asymmetry A_{TL} given by

$$A_{TL} = \frac{\sigma(\phi' = \pi) - \sigma(\phi' = 0)}{\sigma(\phi' = 0) + \sigma(\phi' = \pi)}. \quad (4)$$

One can see from eq. (2) that this observable is closely related to R^{TL} , but it is free from the scale factor ambiguity.

A. Relativistic Distorted Wave Impulse Approximation (RDWIA)

In this paper we restrict ourselves to a kinematical regime that corresponds to quasifree kinematics where the scattering process is strongly dominated by the one-body nucleon current given in eq. (1). Within the relativistic framework the bound nucleon wave function, ψ_B , is a four-spinor with well defined angular momentum quantum numbers κ, μ , corresponding to the shell under consideration. In coordinate space it is given by:

$$\psi_\kappa^\mu(\vec{r}) = \begin{pmatrix} g_\kappa(r) \phi_\kappa^\mu(\hat{r}) \\ i f_\kappa(r) \phi_{-\kappa}^\mu(\hat{r}) \end{pmatrix}, \quad (5)$$

which is eigenstate of total angular momentum with eigenvalue $j = |\kappa| - 1/2$,

$$\phi_\kappa^\mu(\hat{r}) = \sum_{m,\sigma} \langle lm \frac{1}{2} \sigma | j \mu \rangle Y_{l,m}(\hat{r}) \chi_\sigma^{\frac{1}{2}} \quad (6)$$

with $l = \kappa$ if $\kappa > 0$ and $l = -\kappa - 1$ if $\kappa < 0$. The functions f_κ, g_κ satisfy the usual coupled linear differential equations [7,29].

The wave function for the outgoing proton ψ_F is a scattering solution of the Dirac equation, which includes S–V global optical potentials. This wave function is obtained as a partial wave expansion in configuration space [7,8]:

$$\psi_F(\mathbf{r}) = 4\pi \sqrt{\frac{E_F + M}{2E_F V}} \sum_{\kappa, \mu, m} e^{-i\delta_\kappa^*} i^l \langle l \ m \ \frac{1}{2} \ \sigma_F | j \ \mu \rangle Y_{lm}^*(\hat{P}_F) \psi_\kappa^\mu(\vec{r}), \quad (7)$$

where $\psi_\kappa^\mu(\vec{r})$ are four-spinors of the same form as that in eq. (5). The phase-shifts and radial functions are complex because of the complex potential.

The choice of the current operator \hat{J}^μ is to some extent arbitrary. Here we consider the two most popular choices denoted as CC1 and CC2 [10]:

$$\hat{J}_{CC1}^\mu = (F_1 + F_2) \gamma^\mu - \frac{F_2}{2M} (\bar{P} + P_F)^\mu \quad (8)$$

$$\hat{J}_{CC2}^\mu = F_1 \gamma^\mu + i \frac{F_2}{2M} \sigma^{\mu\nu} Q_\nu \quad (9)$$

where F_1 and F_2 are the nucleon form factors related in the usual way [30] to the electric and magnetic Sachs form factors of the dipole form. The variable \bar{P} in eq. (8) is the four-momentum of the initial nucleon for on-shell kinematics, *i.e.*, $\bar{P}^\mu = (E(p), \vec{p})$ ($E(p) =$

$\sqrt{\vec{p}^2 + M^2}$ and $\vec{p} = \vec{p}_F - \vec{q}$). Note that the CC1 current (8) can be obtained from the operator CC2 (9) replacing Q_ν by $(P_F - \overline{P})_\nu$ and using the Gordon decomposition for the free nucleon case, *i.e.*, assuming that initial and final nucleons satisfy the free Dirac equation. For free nucleons eqs. (8) and (9) are equivalent and, since the current is conserved, the time component can be eliminated by writing it in terms of the third component of the current or vice versa. In RDWIA, final and initial nucleons are off-shell and consequently both expressions of the current operator lead to different results. Moreover, the use of an optical potential to account for inelastic reaction channels breaks gauge invariance in DWIA. Once the current operator has been chosen, one must also specify the gauge choice. Currently, Coulomb, Weyl and/or Landau gauges [31] are commonly used. Each of these choices gives different results and it is not clear how to define criteria that favor one choice over the others, or any other possible gauge choice (see discussion in refs. [17,18,32]). In this work we use the Coulomb gauge throughout.

In summary, within the framework of the relativistic distorted wave impulse approximation, the evaluation of the one-body current matrix element involves the use of 4×4 -operators and 4-spinors with negative energy components.

We can divide the differences between this fully relativistic approach and the standard nonrelativistic one into two categories: *i*) Effects due to the fully relativistic current operator, *i.e.*, 4×4 matrix structure of the 4-vector current operator, compared to the 2×2 matrix structure of the nonrelativistic current operator which is usually expanded in \vec{p}/M . We call these effects *kinematical* because they are in principle independent of the dynamics introduced by the nuclear interaction. *ii*) Effects due to the differences between relativistic and nonrelativistic nucleon wave functions, which of course depend not only on the 4-spinor versus 2-spinor structure, but also on the potentials used in the respective Dirac and Schrödinger equation. Thus we call these effects *dynamical*.

Further insight into these differences can be gained recalling the steps taken in nonrelativistic approaches. First, the one-body current operator is expanded in a basis of free-nucleon plane-waves, which amounts to a truncation of the nucleon propagator that ignores negative-energy solutions of the free Dirac equation. This is common to PWIA and DWIA. Second, to take into account (spin-dependent) final-state interactions or distortion effects, in DWIA the current operator is transformed into a 2×2 matrix (usually involving \vec{p}/M expansions) to calculate the nucleon current as the matrix element between the nonrelativistic bound (χ_B) and scattered (χ_F) wave functions. This second step is not needed in PWIA, which can then better incorporate the relativistic kinematics, but misses important absorption effects. A “relativized” form of the 2×2 current operator was proposed in [16,28,33] to optimize the \vec{p}/M expansion.

One may then identify two types of relativistic dynamical effects:

ii – a) Dynamical effects coming from the difference between the upper components of ψ_F (ψ_B) and the solutions χ_F (χ_B) of the Schrödinger equation with standard nonrelativistic potentials. Assuming equivalent central and spin-orbit potentials, this difference stems from the well-known Darwin term. Provided that the relativistic dynamics is known, one can deduce the Darwin term and construct an equivalent bispinor wave function χ to include its effect in the nonrelativistic nucleon current, thus removing this source of differences between relativistic and nonrelativistic results [8,34,35]. This is done for instance in ref. [36]. The influence of this term on $(e, e'p)$ observables has been demonstrated in several

works [7,8,37,38]. In parallel kinematics this appears to be the main dynamical relativistic effect on the cross section in the low- p_m region [7,8], and it is important for the correct determination of the spectroscopic factor from low- p_m data. Its omission reduces the spectroscopic factor by 15–20% in the case of ^{208}Pb and by $\sim 10\%$ in the present case of ^{16}O . Unless explicitly stated, it is included in all calculations presented here.

ii – b) Dynamical effects due to the negative-energy components of the relativistic ψ_B , ψ_F wave functions. Starting from Schrödinger-like solutions χ one may at best construct properly normalized four-spinors of the form

$$\psi = \frac{1}{\sqrt{N}} \left(\chi, \frac{\vec{\sigma} \cdot \vec{p}}{E(p) + M} \chi \right) \quad (10)$$

to calculate the relativistic nucleon current. However, this four-spinor lacks the dynamical enhancement of the lower component of the Dirac solution due to the relativistic S-V potentials. This dynamical enhancement is contained in the negative-energy components of the relativistic ψ_B (ψ_F) solutions and influences $(e, e'p)$ observables in the high- p_m region [8,17]. A discussion of how this effect may be incorporated in nonrelativistic formulations based on 2×2 matrix \vec{p}/M expansions of current operators modified to include the effects of the relativistic S-V potentials can be found in [39].

B. Projected calculation

The sensitivity of the different scattering observables to the negative energy components can be analyzed by constructing properly normalized 4-spinors of the form in eq. (10). Then, one can compare the results obtained using the fully relativistic amplitude given in eq. (1) with those obtained when the negative energy components are projected out. This is done when the nucleon current is calculated as

$$J_{(++)}^\mu(\omega, \vec{q}) = \int d\vec{p} \bar{\psi}_F^{(+)}(\vec{p} + \vec{q}) \hat{J}^\mu(\omega, \vec{q}) \psi_B^{(+)}(\vec{p}), \quad (11)$$

where $\psi_B^{(+)} (\psi_F^{(+)})$ is the positive-energy projection of ψ_B (ψ_F), i.e.,

$$\psi_B^{(+)}(\vec{p}) = \Lambda_{(+)}(\vec{p}) \psi_B(\vec{p}), \quad \psi_F^{(+)}(\vec{p} + \vec{q}) = \Lambda_{(+)}(\vec{p} + \vec{q}) \psi_F(\vec{p} + \vec{q}), \quad (12)$$

with

$$\Lambda_{(+)}(\vec{p}) = \frac{M + \overline{P}}{2M}. \quad (13)$$

The dynamical enhancement of the lower components is contained in the current of eq. (1), but not in eq. (11). It is important to realize that the positive-energy projectors inserted in eq. (11) depend on the integration variable \vec{p} . One could also neglect this \vec{p} -dependence by using projection operators corresponding to asymptotic values of the momenta, *i.e.*, projectors acting on ψ_F and ψ_B respectively, with $P_F^\mu = (E_F, \vec{p}_F)$, $P_B^\mu = P_F^\mu - \overline{Q}^\mu$ the asymptotic four-momentum of the outgoing and bound nucleon respectively, with $\overline{Q}^\mu = (\overline{\omega}, \vec{q})$ and $\overline{\omega} = E_F - \sqrt{(\vec{p}_F - \vec{q})^2 + M^2}$. We refer to this approach

as *asymptotic projection*. This is almost equivalent to the “EMA-noSV” procedure employed in ref. [36], in which a 4-spinor similar to the one given in eq. (10) is used, where the bispinor χ is made identical to the upper component of the Dirac equation solution, but the lower component is obtained with an additional approximation, the effective momentum approach (EMA). This amounts to approximate the value of \vec{p} in eq. (10) by \vec{p}_{as} , with \vec{p}_{as} the momentum corresponding to the asymptotic kinematics at the nucleon vertex. Although the EMA-noSV approach also neglects the enhancement of the lower components, it is not at all equivalent to the exact projection method in eqs. (11,12). The EMA-noSV approach computes the nucleon current with four-spinors that have the same structure than the ones encountered in the scattering of free nucleons, because it enforces the relationship between upper and lower components to be driven by the asymptotic value of the momenta at the nucleon vertex. In particular, the Gordon transformation is exact for the EMA-noSV approach. Therefore, CC1 and CC2 operators would lead to identical results within EMA-noSV, provided the same choices for the off-shell values of ω , E , E_F , \vec{p} and \vec{p}_F are made. This would be a strong prerequisite to a factorized calculation, though still not a sufficient condition. Although we do not show in the figures that follow the results obtained within the EMA-noSV in order to keep the drawings in section III clear enough, we shall comment how this approach compares with the fully relativistic and/or the projected one.

C. Nonrelativistic calculation

In standard nonrelativistic calculations, as the ones presented in [21] based on the computer code DWEEPY [40], besides the truncation into the positive energy space, one must use a suitable 2×2 current operator and 2-component spinors. The nonrelativistic reduction of the 4×4 operator can be performed with a Foldy-Wouthuysen procedure (FW), starting from the relativistic Hamiltonian that represents the interaction of a photon with free nucleons, up to the desired order in $1/M$. In early years, the expansions were done treating at the same footing the 3-momenta of the initial and final nucleon, as well as ω and \vec{q} . Hence, the nonrelativistic Hamiltonian appeared truncated also in powers of ω/M and \vec{q}/M [41]. In present quasielastic ($e, e'p$) experiments the transfer momentum, \vec{q} , can be close or even larger than the nucleon mass, therefore, expansions in \vec{q}/M and/or ω/M must be avoided (see discussion in ref. [16]).

To estimate the effect of truncation of the operator we compare the results obtained with the code DWEEPY used in refs. [21,22] with corresponding results obtained with a non truncated operator. To simplify the comparison, we chose thest cases in plane waves for the ejected nucleon (PWIA). In the plane wave limit, the results of our relativistic code and those of DWEEPY code only differ due to the truncation of the current operator in DWEEPY, provided that in the relativistic formalism we use four-spinors ψ of the form given in eq. (10), whereas in DWEEPY code we introduce as wave function the same bispinor χ of eq. (10). Taking into account a proper normalization of the spinors, the resulting cross-sections for these PWIA benchmarks factorize into phase-space (K), and recoil factor (f_{rec}), electron-proton cross-section (σ_{ep}) and momentum distribution ($n(p) = |\chi(\vec{p})^\dagger \chi(\vec{p})|$) of the single-particle state [1,33]. This provides an additional test of the calculations, because the reduced cross-sections $\rho(p)$ given in eq. (3) must be identical to the momentum distribution $n(p)$, provided the current operator used to obtain σ_{ep} in eq. (3) is the same used to compute

the $(e, e'p)$ cross-section. In the case of the DWEEPY code the truncated current operator was originally derived from the CC2 current operator [40,42], thus in order to perform this tests and obtain $\rho(p)$, a σ_{CC2} version of the σ_{ep} cross-section was factorized out from the PWIA $(e, e'p)$ cross-section.

We stress that within PWIA factorization is recovered if the bound state wave function is of the form in eq. (10). In this case the results for $\rho(p)$ of our code, that uses the full current operator, departed from the momentum distribution $n(p)$ by less than 1% for all the kinematical setups studied in this work. During these tests, the corresponding results of DWEEPY code showed visible differences, as discussed next in section III-C.

III. RESULTS AND DISCUSSION

In this section we present results for cross sections, response functions and left-right asymmetries corresponding to $^{16}O(e, e'p)$ reaction analyzed at different kinematics. We consider the low- $|Q^2|$ experiments carried out at Saclay [20] and NIKHEF [21,22]. We comment briefly the variations introduced by different relativistic nuclear models, optical potentials and prescription for the current operator. In order to make more clear the presentation we discuss our results in several subsections. In the first one we compare our calculations to the experimental reduced cross sections. A detailed discussion on the spectroscopic factors obtained and their sensitivity to the ingredients of the calculation is also presented. In the second subsection we focus on the analysis of the response functions and left-right asymmetry. A third subsection is devoted to a comparison with nonrelativistic calculations, focusing on the TL response.

In this work we consider three data sets that correspond to kinematical conditions of three different experiments:

Set (a) corresponds to the experiment of Leuschner *et al.* at the Medium Energy Accelerator (MEA) at NIKHEF-K [22]. The coincidence reaction $^{16}O(e, e'p)^{15}N$ was analyzed in quasielastic parallel kinematics at three different beam energies: 304, 456 and 521 MeV. The total kinetic energy of the outgoing proton was around 90 MeV. The spectral function of ^{16}O was measured in the range, $0 < E_m < 40$ MeV and $-180 < p_m < 270$ MeV/c, where E_m and p_m are the missing energy and missing momentum, respectively.

Set (b) corresponds to the experiment performed at the Saclay Linear Accelerator by Chinitz *et al.* [20]. The kinematical setup was constant $|\vec{q}| - \omega$ kinematics. The electron beam energy was $\varepsilon = 580$ MeV, the outgoing proton kinetic energy $T_F = 160$ MeV, and the transfer momentum and energy, $|\vec{q}| = 570$ MeV/c and $\omega = 170$ MeV (corresponding to $|Q^2| = 0.3$ (GeV/c) 2). The missing energy resolution was 1.3 MeV, which does not make possible to resolve the $(5/2^+, 1/2^+)$ doublet at an excitation energy $E_x = 5.3$ MeV in ^{15}N from the $3/2^-$ state at $E_x = 6.3$ MeV.

Finally, **set (c)**, also in $|\vec{q}| - \omega$ constant kinematics, was performed by Spaltro *et al.* [21] with the two high-resolution magnetic spectrometers at the medium-energy electron accelerator MEA of NIKHEF-K. Data were measured at momentum and energy-transfer values centered at $(\omega, |\vec{q}|) = (90 \text{ MeV}, 460 \text{ MeV/c})$, *i.e.*, close to the center of the quasielastic peak at $|Q^2| \simeq 0.2$ (GeV/c) 2 . The experiment covered a missing momentum range from 30 to 190 MeV/c. The missing energy resolution was about 180 keV, which made it possible to resolve the $(5/2^+, 1/2^+)$ doublet from the $3/2^-$ state.

A. Reduced Cross Section and spectroscopic factors

In this section we discuss the cross sections measured in the above described $(e, e'p)$ experiments on ^{16}O at low $|Q^2|$ -values. We start with the experiment performed by Leuschner et al. [22], set (a). Note that because of parallel kinematics, for this set the only response functions that contribute to the cross section are R^L and R^T .

Spectroscopic factors for each of the two strong $1p$ transitions are evaluated by scaling the theoretical calculations to the experimental data. They are listed in Table I for different choices of the bound nucleon wave function and current prescriptions. Within parenthesis the statistical error for the spectroscopic factors is listed. The quality of the fit is evidenced by the χ^2 values also quoted in Table I.

Figure 1 shows the reduced cross-section for $p_{1/2}$ and $p_{3/2}$ shells. Results on the right panel correspond to bound state wave function calculated using the parameters of the set NLSH [43]. Results with the older HS set [11,44], as well as with the newest NL3 one [45] are similar. For the scattered proton wave function we use the energy-dependent A -independent potentials derived by Clark *et al.* [12] for ^{16}O . We have verified that using other relativistic optical potentials does not alter significantly our results and conclusions. The sign of p_m refers to the projection of the initial nucleon momentum along the direction of the transfer momentum \vec{q} . It is defined to be positive for $|\vec{q}| < |\vec{p}_F|$ and negative for $|\vec{q}| > |\vec{p}_F|$. Fully relativistic calculations using the CC1 and CC2 current operators (RCC1, RCC2) are shown by thin and thick lines respectively. Throughout this paper we use the Coulomb gauge. The Landau gauge produces similar results because gauge ambiguities are rather small for the fully relativistic results [17,18] and these two gauges.

The role played by relativistic dynamical effects is also analyzed from the results presented in Figure 1. The reduced cross sections evaluated after projecting the bound and scattered proton wave functions over positive energy states (see eq. (11)) are shown by thin-dashed (PCC1) and thick-dashed (PCC2) lines. Note that the difference between PCC1 and PCC2 results is very small because the so-called Gordon ambiguities are reduced after projection [17,18]. The results obtained using the asymptotic values of the momenta in the projection operator as described in section II-B, are almost identical to the PCC2 results and thus are not shown here. Once the global scale factor is taken into account, all the calculations predict a very similar behavior, what indicates that, aside from the Darwin term, the effect of relativistic dynamics (*ii-b*) in the reduced cross-sections is not very important in parallel kinematics at low values of $|Q^2|$.

However, it is apparent from the results in the right panel of Figure 1 that the bound nucleon wave functions do not give correctly the square mean radii for the $p_{1/2}$ and $p_{3/2}$ shells. Note that, whereas the calculations underestimate the maxima, they go above the data on the tails. This comment also applies to the wave functions evaluated with the sets HS and NL3 for the $p_{3/2}$ shell. In the case of the $p_{1/2}$ orbit, the newest NL3 set gives similar results to the NLSH one, whereas the wave function corresponding to the older HS set reproduces better the data. The relativistic Lagrangians NL3, HS, NLSH, are fitted to bulk properties of a few nuclei and it is not surprising that the predicted *r.m.s.r.* values for the ^{16}O orbitals are slightly different than shown in experiment. The wrong *r.m.s.r.* value produces large uncertainties in the determination of spectroscopic factors. This can be seen from the large χ^2 values in the NLSH fit to set (a) data in Table I (similar results

are obtained with the other relativistic Lagrangians mentioned above). The quality of the fits is even worse for the (b) and (c) data sets.

Compared to data sets (b) and (c), data set (a) has many more data points. Indeed, this data set can be reliably used to determine *both* spectroscopic factors and *r.m.s.r.* values. We have therefore adopted the following strategy: First, we use data set (a) to slightly tune the parameters of the NLSH potential so as to reproduce the experimental binding energies and *r.m.s.r.* values of the $p_{1/2}$ and $p_{3/2}$ orbitals in ^{16}O . We denote by NLSH-P the new relativistic potentials and wave functions (see table II). These new relativistic wave functions are then used to make predictions for the kinematical conditions of data sets (b) and (c).

The NLSH-P wave functions are obtained by changing the parameters of the NLSH Lagrangian so that the radii and depth of the S and V potential wells derived from the Lagrangian are modified in the same proportion. The negative energy content of the resulting bound state wave function is barely changed by this procedure. The rescaling of the depth size and radii of the NLSH-P wells is within 10% of the initial NLSH ones. The results for spectroscopic factors, binding energies and *r.m.s.r.* values (both in *p* and *r*-space) are shown in Tables I and II. In particular one can see that the *r.m.s.r.* values are larger in *r*-space (smaller in *p*-space) and produce a much better fit in determining the spectroscopic factors. The χ^2 values are small, the spectroscopic factors have small uncertainty and the curves shown in the left panel of Figure 2 (NLSH-P) follow much more closely the data than those corresponding to NLSH. Systematical errors are not included in Table I. For this experiment the systematical uncertainty of the reduced cross section is 5.4% [22].

As it was the case for the NLSH wave functions, we see in Figure 1 that with the new wave functions NLSH-P, the projected reduced cross sections are very similar to the fully relativistic results. This observation agrees with results of some previous works [15,17,18] where we saw that the dynamical enhancement of the lower component makes an important effect in the cross-section mainly at high missing momentum values and/or in the R^{TL} response function (which *does not contribute in parallel kinematics*), whereas its influence on R^L and R^T is quite modest.

Note that the different curves in Figure 1 are scaled with the spectroscopic factors listed in Table I. From this table we can analyze the uncertainty associated to the use of different prescriptions for the current operator. Notice that the statistical error associated with the spectroscopic factor derived from the NLSH-P wave functions is much smaller. Comparing the fully relativistic results with NLSH-P wave functions for CC1 and CC2, one observes that the differences are at most of the order of $\sim 8\%$ for the case of the $p_{1/2}$ shell and 4% for the $p_{3/2}$ one. With regard to the variation in the spectroscopic factors introduced by the projection procedure, it amounts to 8% (2%) in the $p_{1/2}$ shell and to 8% (2%) for the $p_{3/2}$ orbit with the CC1 (CC2) operator. In the case of the projected calculation, we note that the spectroscopic factors are slightly larger than those corresponding to a fully relativistic calculation. This is due to the enhancement of the lower components of the wave functions which is not contained in the projected approximations. Their effect is enhanced by the CC1 choice. The negative energy components have a smaller effect on the CC2 results. The spectroscopic factors we obtained within the EMA-noSV approximation are almost identical to the PCC2 ones. We recall that another dynamical relativistic effect, namely the Darwin term, is contained in all the figures shown here and amounts to a 10% reduction of the cross section in ^{16}O for the kinematics discussed in this work. This is comparable to the effect of

the Perey factor included in nonrelativistic DWEEPY calculations.

We have also compared the spectroscopic factors obtained with different parameterizations of the nucleon electromagnetic form factors. In all the cases the differences are at most of the order of $\sim 1\%$. We use throughout in this work the Gari-Krümpelmann parameterization [46].

It is interesting to compare the spectroscopic factors listed in Table I with those obtained from fits with standard nonrelativistic DWIA calculations. In the latest case the extracted factors for various choices of optical potentials are $0.61 \leq S_\alpha \leq 0.63$ for $p_{1/2}$, and $0.50 \leq S_\alpha \leq 0.58$ for $p_{3/2}$ [22]. These values are close (but somewhat larger) than the ones listed in Table I.

A smaller spectroscopic factor is expected for the $p_{3/2}$ shell than for the $p_{1/2}$, because the $p_{3/2}$ strength is known to be fragmented into three states: The state considered here at $E_m = 18.4$ MeV, and two weaker peaks at around 22.0 and 22.7 MeV. According to ref. [22,47] the two higher lying peaks would contain about 10% of the total $p_{3/2}$ strength. The spectroscopic factors determined from data set (a) indicate that, taking this extra 10% contribution into account, there is similar $3/2^-$ and $1/2^-$ spectroscopic strength.

In what follows we use the new bound state wave functions (NLSH-P) to make predictions for other experiments. Note that because data set (a) corresponds to parallel kinematics, we have minimized the possible model dependences in the determination of the radii of the bound state wave function. Indeed, as we have just said, apart from a small difference in the spectroscopic factor, the shape of the reduced cross-sections for this kinematics is not affected by the weight given in the calculation to the lower components. This is mainly due to the fact that the R^{TL} response, the most sensitive to the ingredients of the calculation, does not contribute in parallel kinematics. Thus we have used high quality data to fix the size of the wave function but no experimental information on the R^{TL} response has been employed.

Let us now focus on the data sets (b) and (c). Figure 2 shows the reduced cross section for $p_{1/2}$ and $p_{3/2}$ shells. Left and right panel correspond respectively to data sets (b) and (c). As in Figure 1, in each panel we present four curves: thin solid (RCC1), thick solid (RCC2), thin-dashed (PCC1) and thick-dashed (PCC2). For each curve a global scale factor has been fitted to the experimental data. The corresponding scale factors and their statistical errors are listed in Table III. Similarly to what we saw for set (a), also for sets (b) and (c) EMA-noSV results are almost identical to PCC2 ones and thus are not displayed.

The results for the $p_{3/2}$ shell corresponding to the Saclay experiment (data set (b), left panel) include the contribution of the $(5/2^+, 1/2^+)$ doublet. We have verified that the change in the shape of the responses or reduced cross-section after inclusion of the doublet is small. The main effect of its inclusion is a decrease of the deduced spectroscopic factor for the $p_{3/2}$ shell of the order of 10%. In ref. [20] the contribution of this doublet was subtracted from the experimental data with a procedure based on a nonrelativistic formalism. We have chosen to use the uncorrected data from ref. [47], and include the contribution from the doublet in our theoretical calculation. The $s - d$ content has been determined through fits to data set (a) for this state [22]. We determine the spectroscopic factors for the doublet with a procedure similar to the one explained before for the NLSH-P set. The radial size of the S-V potentials is varied by the same amount, while the depth of both potentials is rescaled also by the same factor in order to reproduce the experimental

separation energies of the bound protons. The spectroscopic factors are then obtained by fitting to the data of ref. [22]. The results of the fit are shown in Figure 3. The values of the spectroscopic factors are $S_{1/2+} = 0.040 \pm 0.002 \pm 0.002$ (RCC1), $0.038 \pm 0.002 \pm 0.002$ (RCC2), $S_{5/2+} = 0.087 \pm 0.005 \pm 0.004$ (RCC1), $0.090 \pm 0.005 \pm 0.004$ (RCC2). The quality of the fit is very good, with a χ^2/dof of the order of 0.5. The first uncertainty is statistical, and includes the fact that spectroscopic factors of both states in the doublet are strongly correlated, thus one can obtain essentially the same fit by reducing $S_{1/2+}$ about a 4% and simultaneously increasing $S_{5/2+}$ in approximately the same amount. The second uncertainty is systematical. This procedure to estimate the $s - d$ content is similar to the one used in the nonrelativistic analysis of ref. [22].

Notice that data sets (b) and (c) have fewer points than set (a), and that the error bars are larger. As already mentioned, there is a strong correlation between the *r.m.s.r.* of the bound state wave function and the spectroscopic factor. Thus, trying to fit both the size of the bound state wave function and the spectroscopic factors to either the data set (b) or (c) alone would lead to inconclusive results.

Let us now focus on the results corresponding to data set (b) in left panel of Figure 2. As shown, the calculations reproduce in general the experimental data for both shells with the scale factor listed in Table III. We recall that these reduced cross-sections include the contribution from the doublet, both in our theoretical curves and in the experimental data from ref. [47]. One can observe that the cross sections up to $p_m = 250$ MeV/c do not show an important sensitivity to the negative energy components. Although the various approximations give similar results, we note that the RCC1 reduced cross sections for the $p_{1/2}$ shell are less symmetrical around $p_m = 0$, a behavior that is not favored by the data. We remind that these are *reduced cross-sections* and that the asymmetry around $p_m = 0$ of the reduced cross-sections is *additional* to that already present in σ_{CC1} . It seems that, for data set (b) all the calculations except RCC1 (thin solid line) for the $p_{1/2}$ shell, reproduce well the asymmetry of the reduced cross-section. We will return to this point when talking about the TL observables in next section.

Finally, it is important to remark that the spectroscopic factors obtained from the data set (a) (Table III) agree, within statistical errors, with those obtained from data set (b) for the $p_{1/2}$ shell, but not for the $p_{3/2}$ one. Taking into account the systematic error of both experiments (around 5.4% for data set (a) [22] and 6.3% for data set (b) [47]) the values of the scale factor for the $p_{3/2}$ shell are: $0.43 \pm 0.01 \pm 0.02$ ($0.45 \pm 0.01 \pm 0.03$) for set (a) and $0.49 \pm 0.02 \pm 0.03$ ($0.51 \pm 0.02 \pm 0.03$) for set (b) with RCC1 (RCC2) calculations. Values derived from data set (a) are smaller, and have smaller statistical error than the ones derived from data set (b).

Right panel of Figure 2 corresponds to the data set (c) [21]. The systematic error for data set (c) reduced cross-section is 6% [21]. The scale factors are also listed in Table III. The reduced cross-sections have been obtained from the differential cross-sections and detailed kinematics setup in Appendices A and D of ref. [48]. Concerning the $p_{1/2}$ shell, the reduced cross section is well reproduced by both relativistic and projected calculations, except in the case of the RCC1 calculation (thin solid line) that underestimates the data for negative missing momentum values. This is consistent with the results previously discussed for data set (b). For this shell, the spectroscopic factors that fit data set (c) are larger than the ones derived from data sets (a) or (b), but they are all compatible within statistical errors.

In the case of the $p_{3/2}$ shell, although the shape of the cross section is well reproduced by the various calculations, the situation on the spectroscopic factors is clearly different to the previous case (see Table III). For data set (c), the values of the spectroscopic factors that fit the $p_{3/2}$ data on reduced cross-sections are of the order of 25 – 30% larger than the ones obtained from data set (a). These scale factors are also larger than the ones obtained from data set (b), but in this case the discrepancy is of the order of 15%, which is comparable to the combined systematic and statistical error for these values.

The variations in the spectroscopic factors, summarized in Table III, can be seen graphically in Figure 4. Due to the fact that, except for RCC1 $p_{1/2}$ shell, the shape of the reduced cross-sections is well described by all the calculations and data sets, we can assume that the spectroscopic factors derived are reliable. Thus the differences in the $p_{3/2}$ spectroscopic factors obtained with the same ingredients (wave functions, operators and optical potentials) may be attributed either to a global scale variation among the three experiments for the $p_{3/2}$ shell, or to limitations of the theory. Coupled channel contributions or MEC could make a different effect for the three kinematics analyzed in this work.

The cross sections or reduced cross-sections are not the best observable to look for relativistic effects. As noted in previous works [15,17,18], the effect of the negative-energy components of the wave function on the cross section is mainly visible for high missing momenta $p_m \geq 300$ MeV/c. At low-medium values of the missing momentum, $p_m \leq 250$ MeV/c, the cross sections look rather similar for the various approximations considered (Figures 1 and 2) except for the thin solid line (RCC1) in the $p_{1/2}$ shell for $|\vec{q}| - \omega$ constant kinematics. It is then interesting to analyze observables that play a role in $|\vec{q}| - \omega$ constant kinematics, but not in parallel kinematics. That is, the R^{TL} response. We also know that R^{TL} and left-right asymmetry are much more sensitive to relativistic effects [15,17,18]. Thus, in what follows we focus on the study of these observables.

B. Response Functions and left-right Asymmetry

In this section we present results for the response functions and asymmetries and compare them to the data sets (b) and (c) measured at Saclay [20] and NIKHEF [21], respectively. As already mentioned, these two experiments were performed under $|\vec{q}| - \omega$ constant kinematics so that the response R^{TL} and left-right asymmetry A_{TL} can be obtained from the cross sections measured at $\phi_N = 0$ and $\phi_N = \pi$ with the other variables (ω , Q^2 , E_m , p_m) held constant. Moreover, the response functions $R^L + \frac{q^2}{2Q^2}R^{TT}$ and R^T were also determined for data set (c) [21].

Figures 5 and 6 show R^{TL} and A_{TL} for $p_{1/2}$ (upper panels) and $p_{3/2}$ (lower panels) corresponding to set (b) (left panels) and set (c) (right panels), respectively. In each panel we present four curves with the same conventions as in previous figures: RCC1 (thin solid), RCC2 (thick solid), PCC1 (thin-dashed) and PCC2 (thick-dashed). Each R^{TL} curve is scaled with the corresponding spectroscopic factors listed in Table III. Obviously, the asymmetry A_{TL} is independent on the values of the spectroscopic factors. The results for the $p_{3/2}$ shell in bottom-left panel of Figures 5 and 6 include the contribution of the $(5/2^+, 1/2^+)$ doublet as explained in previous section. Although A_{TL} was not obtained in the experiment performed at Saclay (set (b)), we have been able to deduce A_{TL} from the data using the R^{TL} values

as well as the cross-section data taken at bins with values of p_m approximately symmetric, given in [47]. We have interpolated the cross section data to the nearest symmetrical p_m value corresponding to an R^{TL} measured data point. Then, we have deduced the asymmetry from interpolated values of cross-sections in the denominator, and the difference of cross-sections derived from the experimental R^{TL} data in the numerator. The error bars in A_{TL} include only the statistical error in the cross-section data and in R^{TL} , not the one due to the interpolation procedure. The latter is only important for the two points at the smallest p_m values.

For comparison to previous studies in ref. [20,21], in Table IV we quote the factor required to scale the theoretical predictions to the R^{TL} data, additional to the factors in Table III. A value of one in this table would indicate that the same spectroscopic factor fits *both* the reduced cross section and R^{TL} , that is, the TL strength is consistently predicted by the theory.

Let us start our discussion with the comparison with data set (b). From the results shown in Figures 5 and 6, it is clear that the effect of the negative-energy components shows up more in R^{TL} and A_{TL} than in the cross section (Figure 2). In the case of R^{TL} for the $p_{1/2}$ shell (left-top panel), the RCC2 calculation agrees with experimental data within statistical errors, while PCC1 and PCC2 results for R^{TL} (dashed lines) lie about a 30-50% below the data, and the RCC1 calculation (thin solid line) overestimates the R^{TL} response by around 20% (see Table IV). In the case of the $p_{3/2}$ orbit (left-bottom panel), all the approximations predict similar curves: the projected results are closer to fully relativistic ones than for the $p_{1/2}$ shell. The fully relativistic calculations seem to be favored by the data. Moreover, in this shell the variation introduced by the negative energy components is much smaller than for the $p_{1/2}$ shell. This explains also why the difference between RCC1 and RCC2 results is smaller for the $p_{3/2}$ than for the $p_{1/2}$ shell. These results agree with the general conclusion in refs. [15,18] about the behavior of $j = \ell \pm 1/2$ spin-orbit partners.

The asymmetry A_{TL} for both orbits is presented in the left panels of Figure 6 and the comparison with the data is consistent with what has been found for R^{TL} . In the case of the $p_{1/2}$ shell (top-left panel), one can observe that the RCC2 calculation (thick solid line) fits nicely the experimental data. The RCC1 calculation overestimates A_{TL} and the two projected calculations underestimate it. In the case of the $p_{3/2}$ shell (bottom-left panel) the four theoretical results are very close together, and the experimental data is reproduced by all of them.

In the right panels of Figures 5 and 6 we see the results corresponding to data set (c). Most of the comments on data set (b) apply also here, though the data are a bit more scattered and have larger error bars. In the case of the $p_{1/2}$ shell, PCC1 and PCC2 results are very similar and lie below the data; within the fully relativistic calculation the RCC2 result reproduces the data within statistical errors, while RCC1 overestimates them by a 35%. The analysis of the left-right asymmetries shown in the right panels of Figure 6 leads to the same conclusions as those on R^{TL} , although the data appear even more scattered. The RCC1 calculation lies above the data, as could be advanced by the observation of Figure 5 for R^{TL} . The two projected calculations are rather similar and give smaller asymmetry than the fully relativistic ones. The RCC2 calculation is the one that follows more closely the average trend of the data. In the case of the $p_{3/2}$ shell (bottom-right panel), all the calculations underestimate the experimental TL response by around 17-28%, except RCC1

for which the additional factor in Table IV is compatible with one within statistical errors.

In Figure 7 we show the results for the responses $R^L + v_{TT}/v_L R^{TT}$ (top panels) and R^T (bottom panels) for the $p_{1/2}$ and $p_{3/2}$ shells compared to the data from NIKHEF [21]. As in previous cases, each curve is scaled with the spectroscopic factors quoted in Table III and obtained with fits to the reduced cross-sections. Notice that these responses are rather insensitive to dynamical enhancement of lower components (see also ref. [17] and Figure 1). The results in Figure 7 indicate that the separated responses are in general well reproduced by the relativistic as well as by the projected calculations for both shells, exception made of the data point at the lowest missing momenta where, as indicated by the large error bars, the L/T separation is more problematic.

Summarizing, for the $p_{1/2}$ shell the RCC1 results provide too much R^{TL} and then also yields a too large A_{TL} asymmetry compared to data. The RCC2 results, on the other hand, agree well with all observables and data sets, and the PCC1 and PCC2 results show a too small R^{TL} and A_{TL} . For the $p_{3/2}$ shell, the theoretical calculations lie much closer together than for the $p_{1/2}$ shell, and generally agree with all data sets and observables, except for R^{TL} and A_{TL} for data set (c), where the data lie a $30\% \pm 10\%$ higher than the PCC1 and PCC2 theoretical calculations, while within statistical errors they are almost compatible with RCC1 and RCC2 calculations. This is certainly at variance with the situation found in ref. [21], and it is worth identifying the reasons for the difference, what we do in the next section.

C. Comparison with former analyses

To compare with the previous nonrelativistic results of ref. [21,22] we start by looking at the effect due to the truncated current operator used in those analyses. We compare in Figure 8 reduced cross sections for the kinematical conditions of sets (a), (b) and (c), obtained in the plane wave limit of our relativistic formalism and of the DWEEPY program. As described in section II-C the solid and dashed curves in Figure 8 differ only due to the truncation of the current operator employed in DWEEPY.

We can see that for kinematics (a) the full operator and the one in DWEEPY yield essentially identical results for the $p_{1/2}$ shell, and slightly different ones for the $p_{3/2}$. The difference is less than 2% in any case, and therefore the truncated operator employed in the analyses of ref. [22] does not explain the differences with the full relativistic analysis of our work for set (a). We conclude that the determination of the spectroscopic factor and the *r.m.s.r.* of the bound state wave function made in ref. [22] was not affected by the use of a truncated operator instead of the complete one.

For set (c), the differences in the reduced cross-section are still small, but they are more important for $p_m < 0$ where they amount to 5%. This indicates that the effect of truncation will be more important for R^{TL} or A_{TL} observables than for the reduced cross-section. For set (b), the effect of truncation is important in the whole p_m range, but again more sizeable for $p_m < 0$ (10%) than for $p_m > 0$ (5%). If one tries to deduce spectroscopic factors from results obtained with the truncated operator, they should be a 10% (5%) larger for set (b) ((c)).

In Figure 9 we plot R^{TL} and A_{TL} for the kinematics (b) (left) and (c) (right). This figure shows that with the truncated operator, R^{TL} and A_{TL} are underestimated by 15% for set

(b) and 11% for set (c).

Next we comment in detail (point by point) the differences between our procedure and that of Spaltro *et al.* in ref. [21] concerning the analyses of R^{TL} responses.

1. First of all, the scale factors are different. While in ref. [21] the scale factors were taken from the work of Leuschner *et al.* [22], we have derived spectroscopic factors for each of the three data sets ((a), (b) and (c)) using the data on reduced cross sections. This is important because the scale factors are not free from errors and ambiguities. There are statistical and systematical errors (both of the order of 5%-6%). Particularly, there is a normalization uncertainty in the cross-sections. This uncertainty affects in the same way the response functions and cross-sections inside a single data set, but when comparing two different data sets, a 5% systematical error could translate into a 10% difference of the cross-sections and corresponding scale factors. This difference may lead to inconsistencies when comparing the R^{TL} response from one data set using the scale factor derived from a different data set. As one can see from Figure 4 and Table III, this different choice of spectroscopic factors would introduce only a small difference with respect to the choice we make in this work for the $p_{1/2}$ shell. Note that in this case all the scale factors we derive from the three data sets are compatible within statistical errors. For the $p_{3/2}$ shell, however, this different choice of spectroscopic factors would affect much more the R^{TL} comparisons because there is a $27\% \pm 6\%$ difference between the scale factors derived from data sets (a) and (c). Taking into account both systematical and statistical errors, the scale factors derived in this work from these two data sets differ by two standard deviations, while the ones derived from data set (b) lie in between the other two, and are compatible with both of them. As the 27% difference is present only for the $p_{3/2}$ shell, it is probably too simplistic attributing it to a normalization problem of some or all of the data sets. Note that, for instance, reducing the spectroscopic factors obtained from data set (c) by a 10%, the values deduced from the three data sets in both shells will be compatible. To settle the issue of a possible normalization problem, we would need more precise experimental information to determine the scale factors with smaller uncertainties. In order to avoid the uncertainty due to the scale factor, one should resort to compare instead, the A_{TL} asymmetry from different experiments.

What is clear is that if we had used the scale factor derived from data set (a) to plot our R^{TL} responses, we would have found almost no difference from the situation depicted in Figure 5 in the case of the $p_{1/2}$ shell. On the contrary, for the $p_{3/2}$ one, the theoretical curves would lie a 26% below the ones that are shown, what would certainly resemble of the situation found in ref. [21].

2. Another difference lies in the use of relativistic operator and wave functions employed in our work, compared to the nonrelativistic ones used in ref. [21]. As discussed in section II-C such differences can be appreciated comparing the RPWIA CC2 results to the ones obtained with the truncated operator employed in DWEEPY. Figures 8 and 9 show that at these kinematics the differences are small but not negligible:
 - (a) The truncated operator employed in refs. [21,22] yields a 10% to 15% smaller R^{TL} response for the kinematics of sets (c) or (b). For the case of data set (a), where

only R^L and R^T responses are involved, we observe that the reduced cross sections in top panel of Figure 8 are almost identical, showing that the effect of truncation for these two responses and for the cross sections is negligible at this kinematics. However, differences of a 5% and larger appear in $|\vec{q}| - \omega$ constant kinematics, due to the contribution of R^{TL} that is more sensitive to the truncation, even at the moderate values of $|Q|^2$ of data sets (b) and (c).

- (b) Apart from the truncation of the operator, the nonrelativistic approach deals only with positive energy spinors. In the relativistic case, due to dynamics, there is a presence of negative energy components in the wave function, this is, an increase of the lower components. This dynamical relativistic effect has a very characteristic signature because its effects are seen specially in the R^{TL} responses, and much more for $j = \ell - 1/2$ shells than for $j = \ell + 1/2$ ones [15,17,18]. After studying the TL observables for the $p_{1/2}$ shell in Figures 5 and 6 we conclude that the RCC2 calculation is favored by the experimental data.

The relative importance of all these ingredients can be seen in Figure 10. In this figure we compare relativistic results RCC2 (solid lines), PCC2 (dashed lines) and nonrelativistic results from ref. [21] (dotted). The important difference between dashed lines and dotted ones, particularly for $p_{3/2}$ shell, can be attributed to the combined effect of the different scale factors and of the truncation of the current operator. Comparison of solid and dashed lines shows the effect of the dynamical enhancement of the lower components.

Finally we comment on the differences with previous analysis of data set (b) in ref. [20]. These data were analyzed in [20] comparing with a RDWIA calculation of Van Orden, similar to our RCC1 calculation, except for the use of a different optical potential and different bound state wave functions. Furthermore, in [20] an attempt to remove the contribution of the doublet from the $p_{3/2}$ cross-section data was done, and the spectroscopic factors were obtained from differential cross sections. The R^{TL} data were found to be a 13(3)% larger than the theory for $p_{3/2}$ and up to 30(6)% larger for $p_{1/2}$. We have checked that part of that discrepancy is due to the values used for the spectroscopic factors. The derivation of spectroscopic factors based upon *reduced cross-sections*, leads to theoretical RCC2 R^{TL} responses that are only $0.98 \pm 0.14\%$ ($p_{3/2}$) and $0.86 \pm 0.11\%$ ($p_{1/2}$) times the experimental data. This improvement is largely due to the proper treatment of kinematical factors for the reduced cross-sections and R^{TL} . In part it is also due to the use of a more modern phenomenological optical potential for ^{16}O and to the use of bound state wave functions that reproduce the *r.m.s.* radius exhibited by the reduced cross-section.

IV. SUMMARY AND CONCLUSIONS

In summary we find that the fully relativistic treatment improves substantially the description of reduced cross-sections and individual responses of all three sets of data on $^{16}O(e, e'p)$ at low $|Q^2|$. Although predictions from CC1 and CC2 current operators are rather close in most cases, data seem to favor the CC2 current operator. Our remarks here focus mainly on results with CC2 and with the improved NLSH-P bound nucleon wave functions, that have the correct *r.m.s.* radius. Using the most complete set of data (in parallel

kinematics) on reduced cross-sections of Leuschner *et al.* [22] (set (a)) we obtain spectroscopic factors of 0.58(1) for $p_{1/2}$ shell and 0.45(1) for $p_{3/2}$. On theoretical grounds [49], such small spectroscopic factors are expected from shell model Monte Carlo calculations on ^{16}O , though other theories predict somewhat larger values [50,51]. Within error bars, these spectroscopic factors are consistent with the ones obtained using the other two sets of data on reduced cross-sections in $|\vec{q}| - \omega$ constant kinematics (set (b) from Chinitz *et al.* [20] and set (c) from Spaltro *et al.* [21]). Exception has to be made of the spectroscopic factor obtained for $p_{3/2}$ from data set (c) [21], which is 25-30% larger than the one obtained from data sets (a) and (b).

There is a long standing controversy surrounding the TL data for the $p_{1/2}$ and $p_{3/2}$ shells measured at Saclay [20] and NIKHEF [21]. We have therefore paid particular attention to TL responses and asymmetries and we conclude that there is not a fundamental inconsistency. The TL response is more sensitive than L and T responses to relativistic effects, in particular to the dynamical enhancement of the lower components. The role played by the latter is appreciated comparing fully relativistic results (RCC2 or RCC1) to those obtained using wave functions projected on the positive energy sector (PCC2 or PCC1). RCC2 results agree well with experimental TL responses on $p_{1/2}$ (as well as with TL asymmetries) which are underestimated by PCC2 and overestimated by RCC1, because CC1 current operator overemphasizes the role of negative energy components. The overall agreement with data on TL responses and asymmetries from set (b) and set (c) is quite satisfactory, with the exception of data on $p_{3/2}$ shell from set (c), but even in this case theory is much closer to experiment than previously found in ref. [21]. In particular, the large difference between data on TL responses from the two different sets is well accounted for by the present analyses. This is in contrast with the situation depicted in ref. [21] (see in particular Figure 2 of ref. [21]). The large general mismatch of data set (c) on $p_{3/2}$ shell seems to point to a normalization problem which would require experimental verification. Our analyses indicates that the problem is not so much connected to the TL response, but rather to the normalization used. Nevertheless, since meson exchange currents and particularly isobar currents are claimed to affect more the $p_{3/2}$ than the $p_{1/2}$ orbitals [24], it would be interesting to see whether our fully relativistic calculation extended to include the isobar and other meson exchange effects would lead to better agreement with TL $p_{3/2}$ data from set (c).

This work was partially supported under Contracts No. PB/98-1111, PB/98-0676, PB/96-0604 and by the Junta de Andalucía (Spain). J.R.V. and A.E. acknowledge support from doctoral fellowships of the Consejería de Educación y Cultura de la Comunidad de Madrid and Ministerio de Educación y Cultura (Spain), respectively.

TABLES

Shell	Operator	NLSH				NLSH-P			
		R		P		R		P	
		S_α	χ^2/dof	S_α	χ^2/dof	S_α	χ^2/dof	S_α	χ^2/dof
$1p_{1/2}$	CC1	0.58(3)	6.6	0.65(2)	4.5	0.54(1)	1.3	0.58(1)	1.2
	CC2	0.64(2)	4.5	0.66(2)	3.2	0.58(1)	1.3	0.59(1)	1.6
$1p_{3/2}$	CC1	0.45(3)	25.3	0.51(3)	16.9	0.43(1)	2.7	0.47(1)	3.6
	CC2	0.49(3)	15.7	0.52(3)	13.3	0.45(1)	3.5	0.46(1)	4.3

TABLE I. Spectroscopic factors derived from Leuschner's experimental reduced cross sections in ref. [22] (data set (a)) using NLSH and NLSH-P relativistic bound nucleon wave functions (see text). The following nomenclature is used: R: fully relativistic calculation. P: relativistic calculation projecting the wave functions over positive energy states. The numbers within parentheses indicate the statistical error. The χ^2 per degree of freedom is also quoted.

$p_{1/2}$			$p_{3/2}$		
	<i>b.e.</i> (MeV)	<i>r.m.s.r.-r</i> (fm)	<i>r.m.s.r.-p</i> (MeV)	<i>b.e.</i> (MeV)	<i>r.m.s.r.-r</i> (fm)
NLSH	11.4	2.838	175.7	18.8	2.679
NLSH-P	12.1	3.043	170.6	18.4	2.907

TABLE II. Comparison of binding energies and *r.m.s.r.* radius in *p*- and *r*- space for the wave functions NLSH [43] and NLSH-P. The contribution from the negative energy components to the norm of the wave function is about 2% in all cases.

Set (a) Leuschner <i>et al.</i> [22]				Set (b) Chinitz <i>et al.</i> [20]				Set (c) Spaltro <i>et al.</i> [21]				
$p_{1/2}$		$p_{3/2}$		$p_{1/2}$		$p_{3/2}$		$p_{1/2}$		$p_{3/2}$		
	CC1	CC2	CC1	CC2	CC1	CC2	CC1	CC2	CC1	CC2	CC1	CC2
R	0.54(1)	0.58(1)	0.43(1)	0.45(1)	0.54(4)	0.56(3)	0.49(2)	0.51(2)	0.57(3)	0.61(2)	0.56(1)	0.59(2)
P	0.58(1)	0.59(1)	0.47(1)	0.46(1)	0.60(5)	0.57(4)	0.54(3)	0.53(3)	0.66(2)	0.63(2)	0.61(1)	0.61(2)
NR	0.61(1)–0.64(1)		0.50(1)–0.59(1)									

TABLE III. Spectroscopic factors derived from three different sets of data on experimental reduced cross sections. The following nomenclature is used: R, fully relativistic calculation; P, relativistic calculations projecting the wave functions over positive energy states; NR, range of values obtained with the nonrelativistic analyses of ref. [22]. The numbers within parentheses show the statistical error only. CC1 and CC2 refer to the choice used for the proton current operator.

	Set (c)				Set (b)			
	$p_{1/2}$		$p_{3/2}$		$p_{1/2}$		$p_{3/2}$	
	N	χ^2/dof	N	χ^2/dof	N	χ^2/dof	N	χ^2/dof
RCC1	0.63(10)	1.1	1.09(12)	3.2	0.83(10)	0.65	0.95(17)	5.3
PCC1	1.15(17)	1.1	1.28(12)	2.5	1.32(42)	4.5	1.14(22)	5.8
RCC2	0.90(13)	1.0	1.17(12)	2.5	1.14(12)	0.49	1.02(15)	3.4
PCC2	1.26(19)	1.0	1.28(11)	2.1	1.48(32)	2.2	1.11(17)	3.8
NR	1.50(12)	—	2.05(10)	—	1.56(12)	—	1.66(9)	—

TABLE IV. Additional scale factors needed to fit the experimental R^{TL} response previously scaled by the corresponding spectroscopic factors in Table III. A value of one would indicate that no extra enhancement or quenching of the response is found. The numbers in parentheses show the statistical error only. The quality of the fit (χ^2/dof) is also quoted in every case. NR corresponds to the nonrelativistic analysis of ref. [21].

REFERENCES

- [1] S. Boffi, C. Giusti, F.D. Pacati, Phys. Rep. **226**, 1 (1993); S. Boffi, C. Giusti, F. Pacati, M. Radici, “*Electromagnetic Response of Atomic Nuclei*”, (Oxford-Clarendon Press, 1996); J.J. Kelly, Adv. Nucl. Phys. **23**, 75 (1996).
- [2] I. Bobeldijk *et al.*, Phys. Rev. Lett. **73**, 2684 (1994).
- [3] L. Lapikás, Nucl. Phys. **A553**, 297c (1993).
- [4] V.R. Pandharipande, C.N. Papanicolas, J. Wambach, Phys. Rev. Lett. **53**, 1133 (1984); Z.Y. Ma, J. Wambach, Phys. Lett. B **256**, 1 (1991); C. Mahaux, R. Sartor, Adv. Nucl. Phys. **20**, 1 (1991).
- [5] H. Müther, W.H. Dickhoff, Phys. Rev. C **49**, R17 (1994).
- [6] V. Van der Sluys, J. Ryckebusch, M. Waroquier, Phys. Rev. C **54**, 1322 (1996).
- [7] J.M. Udías, P. Sarriguren, E. Moya de Guerra, E. Garrido, J.A. Caballero, Phys. Rev. C **48**, 2731 (1993).
- [8] J.M. Udías, P. Sarriguren, E. Moya de Guerra, E. Garrido, J.A. Caballero, Phys. Rev. C **51**, 3246 (1995).
- [9] J.M. Udías, P. Sarriguren, E. Moya de Guerra, J.A. Caballero, Phys. Rev. C **53**, R1488 (1996).
- [10] T. de Forest, Nucl. Phys. **A392**, 232 (1983).
- [11] C.J. Horowitz, D.P. Murdock, B.D. Serot, *Computational Nuclear Physics*, Eds. K. Langanke, J.A. Maruhn, S.E. Koonin (Springer, Berlin, 1991).
- [12] E.D. Cooper, S. Hama, B.C. Clark, R.L. Mercer, Phys. Rev. C **47**, 297 (1993).
- [13] A. Picklesimer, J.W. Van Orden, Phys. Rev. C **35**, 266 (1987); **40**, 290 (1989).
- [14] J.P. McDermott, Phys. Rev. Lett. **65**, 1991 (1990); Y. Jin, D.S. Onley, L.E. Wright, Phys. Rev. C **45**, 1311 (1992).
- [15] J.M. Udías, J.A. Caballero, E. Moya de Guerra, J.E. Amaro, T.W. Donnelly, Phys. Rev. Lett. **83**, 5451 (1999).
- [16] J.E. Amaro, J.A. Caballero, T.W. Donnelly, A.M. Lallena, E. Moya de Guerra, J.M. Udías, Nucl. Phys. **A602**, 263 (1996); J.E. Amaro, J.A. Caballero, T.W. Donnelly, E. Moya de Guerra, **A611**, 163 (1996).
- [17] J.A. Caballero, T.W. Donnelly, E. Moya de Guerra, J.M. Udías, Nucl. Phys. **A632**, 323 (1998).
- [18] J.A. Caballero, T.W. Donnelly, E. Moya de Guerra, J.M. Udías, Nucl. Phys. **A643**, 189 (1998).
- [19] J. Gao *et al.*, Phys. Rev. Lett. **84**, 3265 (2000).
- [20] L. Chinitz *et al.*, Phys. Rev. Lett. **67**, 658 (1991).
- [21] C.M. Spaltro, H.P. Blok, E. Jans, L. Lapikás, M. van der Schaer, G. van der Steenhoven, P.K.A. de Witt Huberts, Phys. Rev. C **48**, 2385 (1993).
- [22] M. Leuschner *et al.*, Phys. Rev. C **49**, 955 (1994).
- [23] P. Schwandt, H.O. Meyer, W.W. Jacobs, A.D. Bacher, S.E. Vigdor, M.D. Kaitchuck, T.R. Donoghue, Phys. Rev. C **26**, 55 (1982).
- [24] J. Ryckebusch, D. Debruyne, W.V. Nespen, S. Janssen, Phys. Rev. C **60**, 034604 (1999).
- [25] J.E. Amaro, A.M. Lallena, J.A. Caballero, Phys. Rev. C **60**, 014602 (1999).
- [26] J.M. Udías, J.R. Vignote, Phys. Rev. C **62**, 034302 (2000).
- [27] A.S. Raskin, T.W. Donnelly, Ann. of Phys. (NY) **191**, 78 (1989).

[28] J.E. Amaro, T.W. Donnelly, Ann. Phys. (NY) **263**, 56 (1998); Nucl. Phys. **A646**, 187 (1999); S. Jeschonnek, T.W. Donnelly, Phys. Rev. C **57**, 2438 (1998).

[29] H. Überall, *Electron Scattering from Complex Nuclei*, Academic, N.Y., (1971). M.E. Rose, *Relativistic Electron Scattering*, Wiley, N.Y., (1961).

[30] J.D. Bjorken, S.D. Drell, *Relativistic Quantum Mechanics*, Mc Graw-Hill, N.Y., (1964)

[31] H.W.L. Naus, S. Pollock, J.H. Koch, U. Oelfke, Nucl. Phys. **A509**, 717 (1990); S. Pollock, H.W.L. Naus, J.H. Koch Phys. Rev. C **53**, 2304 (1996).

[32] J.A. Caballero, T.W. Donnelly, G.I. Poulis, Nucl. Phys. **A555**, 709 (1993).

[33] S. Jeschonnek, nucl-th/0009086; S.Gardner, J.Piekarewicz, Phys.Rev. C **50**, 2882 (1994).

[34] S. Hama, B.C. Clark, E.D. Cooper, H.S. Sherif, R.L. Mercer, Phys. Rev. C **41**, 2737 (1990).

[35] G.H. Rawitscher, Phys. Rev. C **31**, 1173 (1985).

[36] J.J. Kelly, Phys. Rev. C **56**, 2672 (1997); **59**, 3256 (1999).

[37] S. Boffi, C. Giusti, F.D. Pacati, F. Cannata, Nuovo Cimento **98**, 291 (1987).

[38] Y. Jin, D.S. Onley, Phys. Rev. C **50**, 377 (1994).

[39] M. Hedayati-Poor, J.I. Johansson, H.S. Sherif, Phys. Rev. C **51**, 2044 (1995); Nucl. Phys. **A593**, 377 (1995); J.I. Johansson, H.S. Sherif, G.M. Lotz, Nucl. Phys. **A605**, 517 (1996).

[40] C. Giusti, F. Pacati, Nucl. Phys. **A473**, 717 (1987).

[41] K.W. McVoy, L.H. Hove, Phys. Rev. **125**, 1034 (1962).

[42] C. Giusti, F. Pacati, Nucl. Phys. **A336**, 427 (1980).

[43] M.M. Sharma, M.A. Nagarajan, P. Ring; Phys. Lett. B **312**, 377 (1993).

[44] B.D. Serot, J.D. Walecka, Adv. Nucl. Phys. **16**, 1 (1986).

[45] G.A. Lalazissis, J. König, P. Ring, Phys. Rev. C **55**, 540 (1997).

[46] M.F. Gari, W. Krümpelmann, Phys. Lett. B **141**, 295 (1984); Z. Phys. A **322**, 689 (1985); Phys. Lett. B **173**, 10 (1986).

[47] L. Chinitz, Ph.D. Thesis, University of Virginia (1990) (*unpublished*).

[48] C.M. Spaltro, M.Sc. thesis, University of Utrecht (1992) (*unpublished*).

[49] T. Otsuka in "Proceedings of the International NATO-Advanced Study Institute on Nuclei far from Stability and Astrophysics", Poenareau, Rebel, and Wentz, eds. (NATO-ASI Series, 2000), *in press*.

[50] D. Van Neck, M. Waroquier, A.E.L. Dieperink, Steven C. Pieper, V.R. Pandharipande, Phys. Rev. C **57**, 2308 (1998).

[51] W.J.W. Geurts, K. Allaart, W.H. Dickhoff and H. Müther, Phys. Rev. C **53**, 2207 (1996).

FIGURES

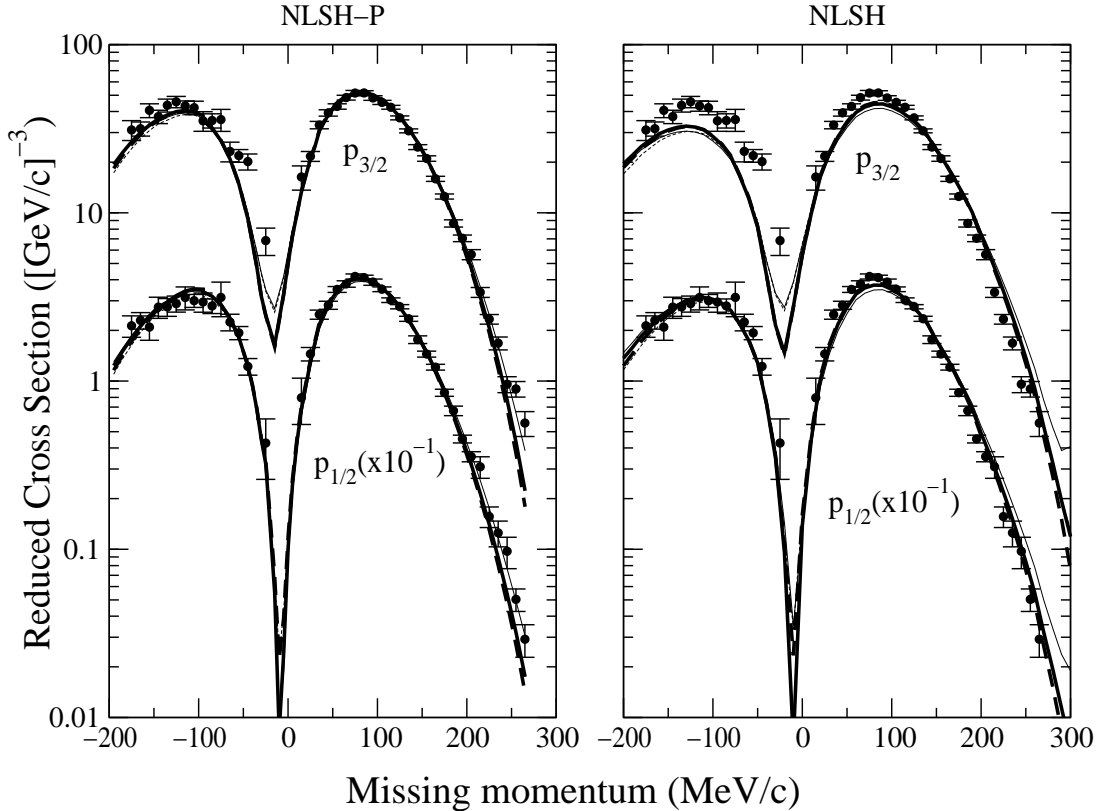


FIG. 1. Reduced cross sections for proton knockout from $1p_{1/2}$ and $1p_{3/2}$ orbits in ^{16}O versus missing momentum p_m corresponding to the experiment performed by Leuschner *et al.* [22] (set (a)). The bound relativistic proton wave function has been obtained with the NLSH (right panel) and NLSH-P (left panel) parameterization. Theoretical results shown correspond to a fully relativistic calculation using the Coulomb gauge and current operators RCC1 (thin solid line) and RCC2 (thick solid line). Also shown are the results after projecting the bound and scattered proton wave functions over positive-energy states: PCC1 (thin dashed line), PCC2 (thick dashed line). EMA-noSV results (not shown) are practically identical to PCC2 ones. Each curve is scaled by the corresponding spectroscopic factor in Table I.

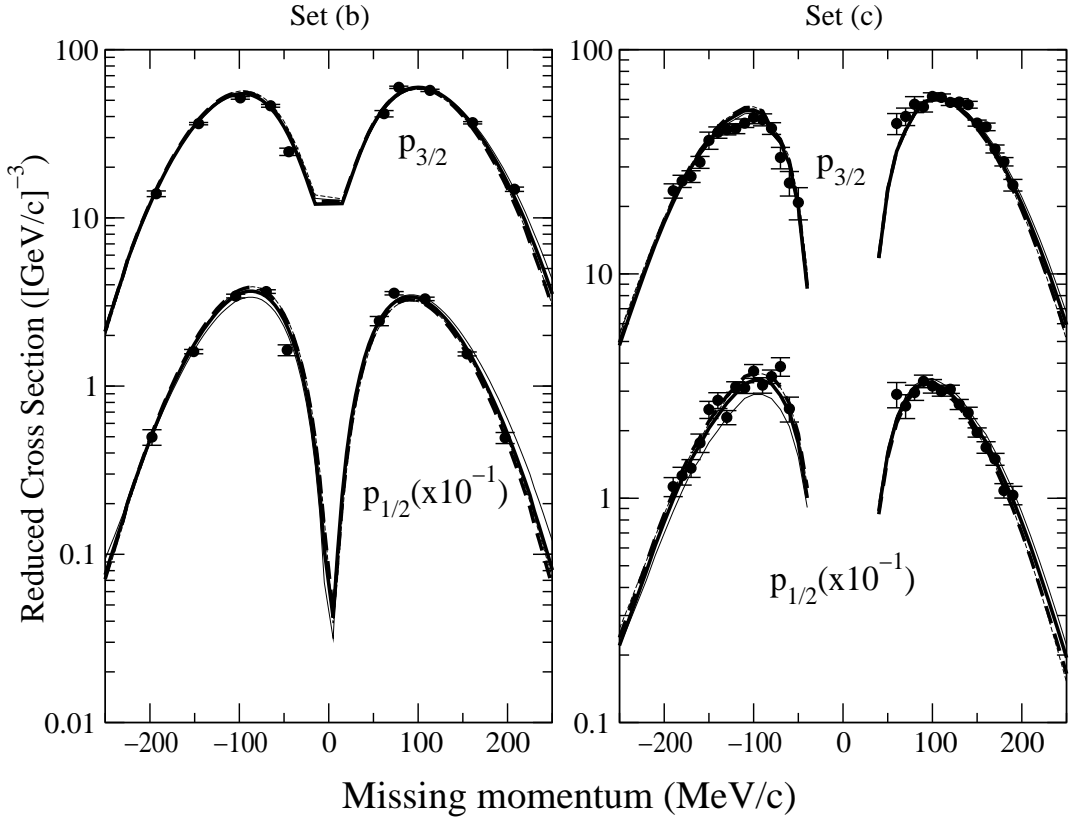


FIG. 2. Same as Figure 1 for the experiments performed by Chinitz *et al.* [20] (left panel, set (b)) and by Spaltro *et al.* [21] (right panel, set (c)). In all the cases the NLSH-P relativistic bound proton wave functions have been used. For $p_{3/2}$ shell in set (b) the contribution from the nearby $5/2^+$ and $1/2^+$ states has been taken into account (see text). Each curve is scaled by the corresponding spectroscopic factor in Table III.

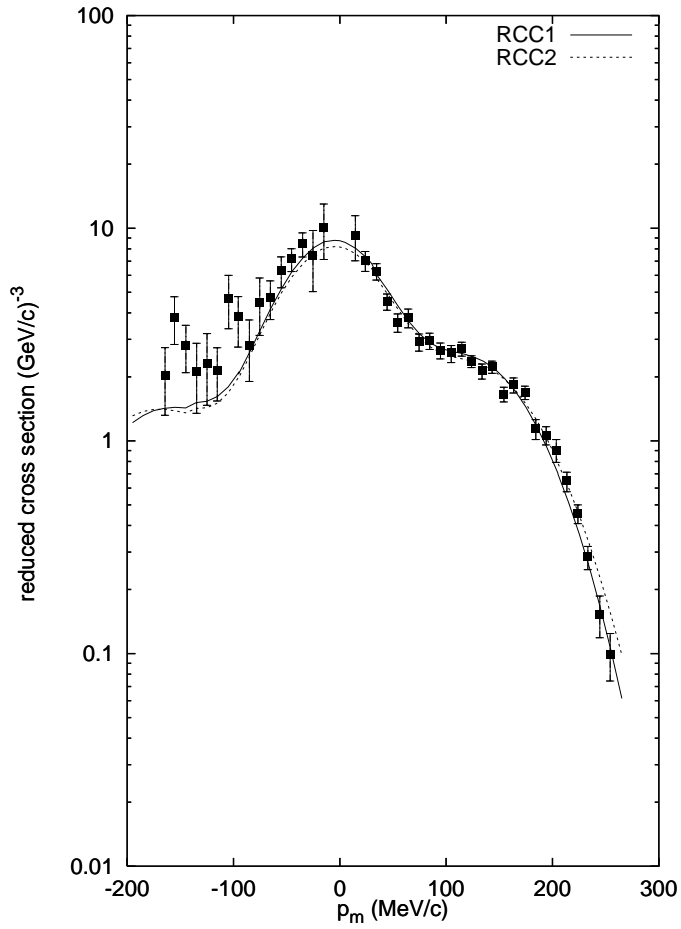


FIG. 3. Reduced cross-sections for the doublet of $5/2^+$ and $1/2^+$ states at $E_m = 17.4$ MeV compared to the experimental data from ref. [22]. Deduced occupancies are $0.034(2)$ $2s + 0.087(5)$ $1d$ with RCC1, and $0.034(2)$ $2s + 0.090(5)$ $1d$ with RCC2.

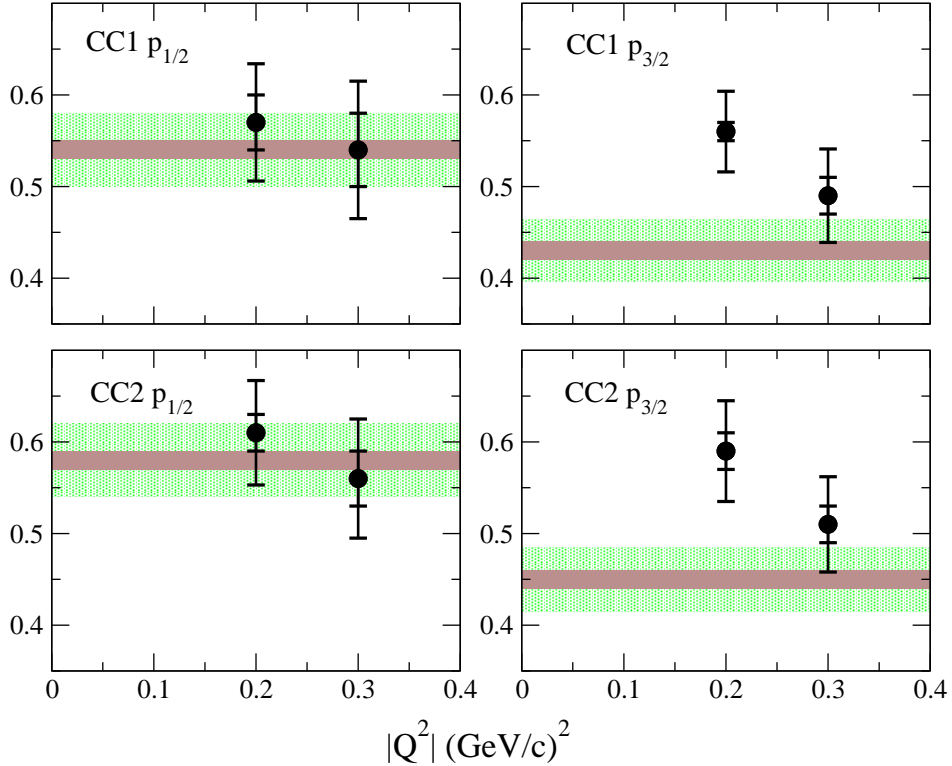


FIG. 4. Spectroscopic factors derived within the fully relativistic approach from the low- Q^2 data discussed in this work. The inner error bars include statistical errors only, the outer one includes also the additional systematic error in the reduced cross-sections for each experiment. The bands covering the whole $|Q^2|$ range corresponds to the value obtained from the data set (a) [22], while the dots at $|Q^2| = 0.2$ (GeV/c^2) and 0.3 (GeV/c^2) correspond to the data set (c) [21] and set (b) [20], respectively.

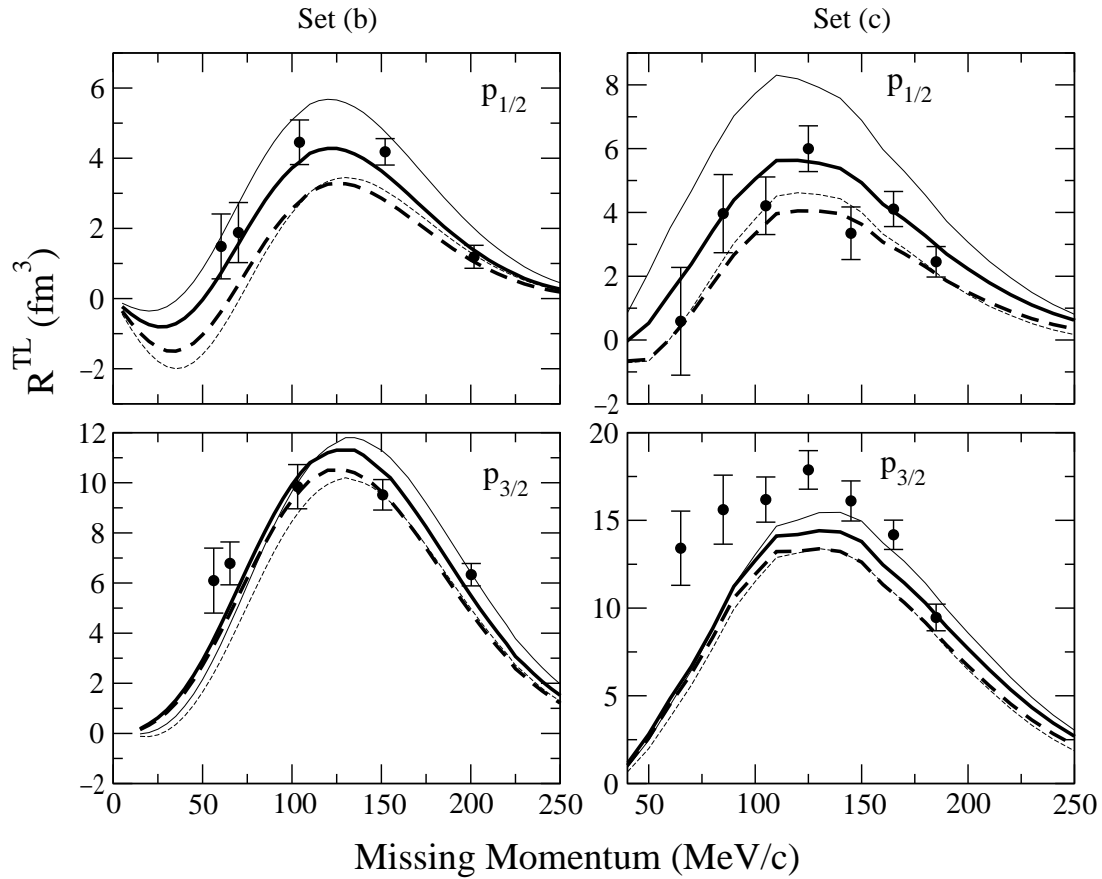


FIG. 5. Response R^{TL} for proton knockout from ^{16}O for $1p_{1/2}$ (top panels) and $1p_{3/2}$ (bottom panels). Results and data shown correspond to kinematics of data set (b) [20] (left) and set (c) [21] (right). Curves as in Figure 2.

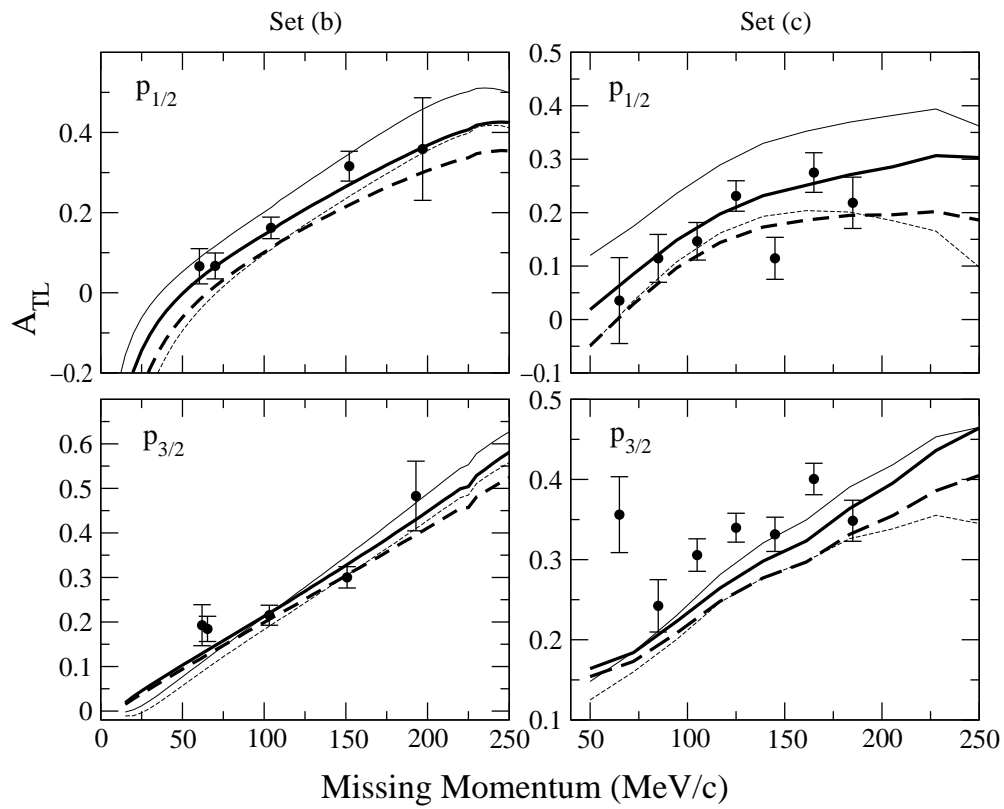


FIG. 6. Same as Figure 5 for the A_{TL} asymmetry.

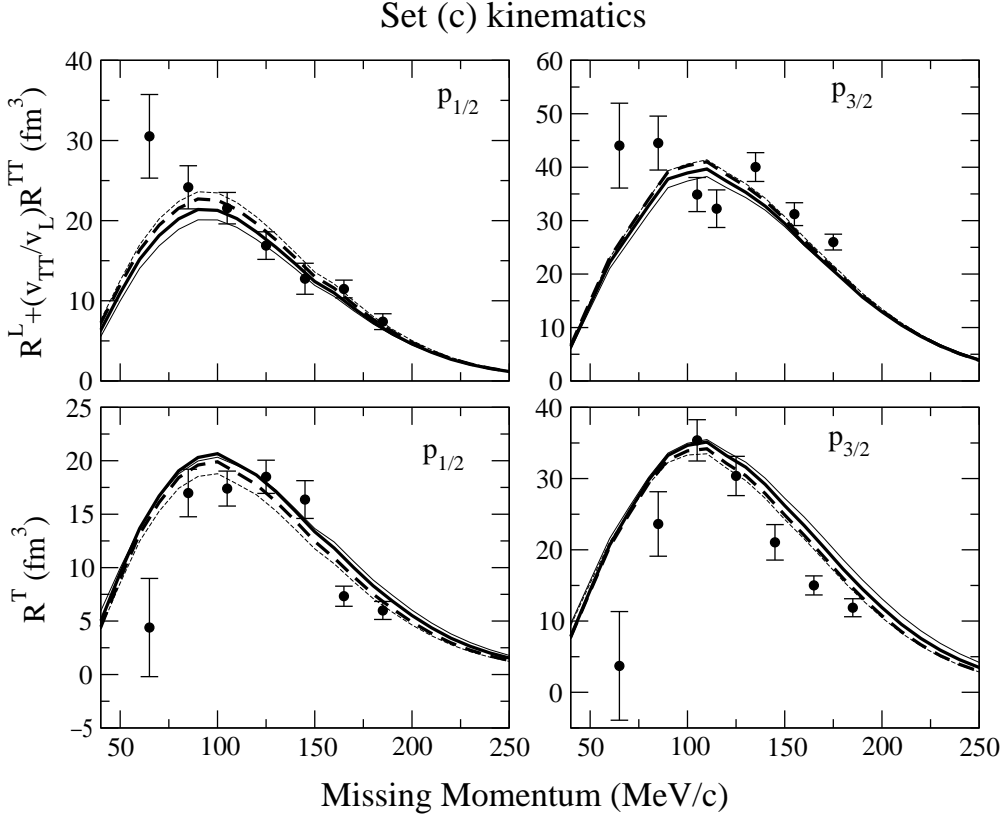


FIG. 7. Response functions $R^L + v_{TT}/v_L R^{TT}$ and R^T for the kinematics of data set (c) [21]. The theoretical results are scaled with the spectroscopic factors for this same experiment in Table III. Solid (dashed) lines correspond to the full relativistic (projected) calculation, thin (thick) lines with the choice CC1 (CC2).

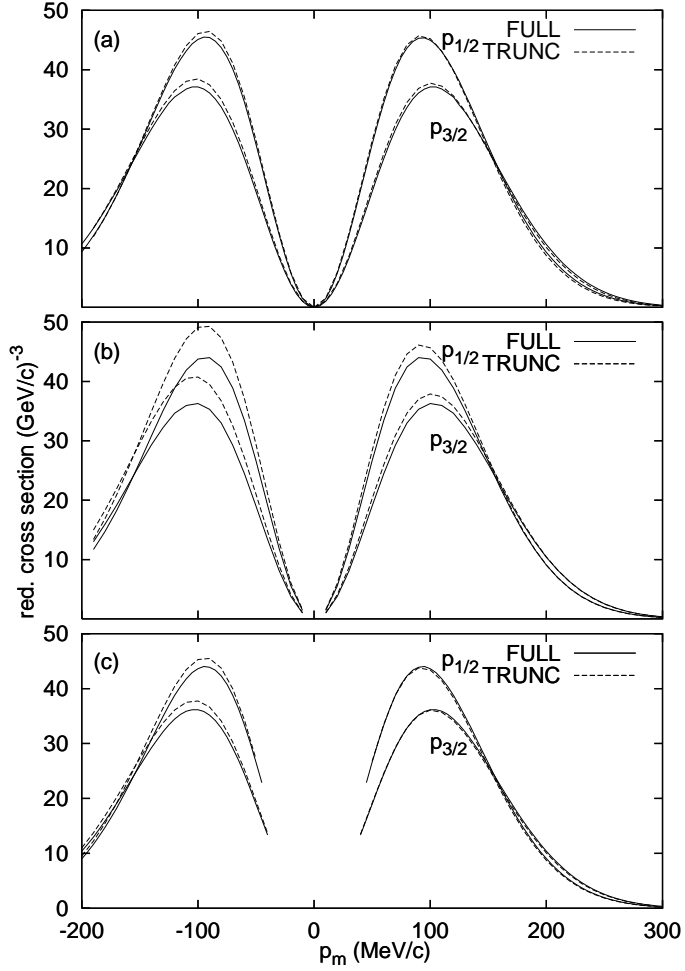


FIG. 8. Effect of truncation of the current operator for the kinematics of sets (a), (b) and (c). In all cases the results are in plane wave limit for the outgoing proton. For the solid lines, we used the relativistic formalism with bound proton wave function ψ of eq. (10) and CC2 current operator. Dotted lines correspond to nonrelativistic results using the equivalent bispinor χ in eq. (10) and the code DWEEPY.

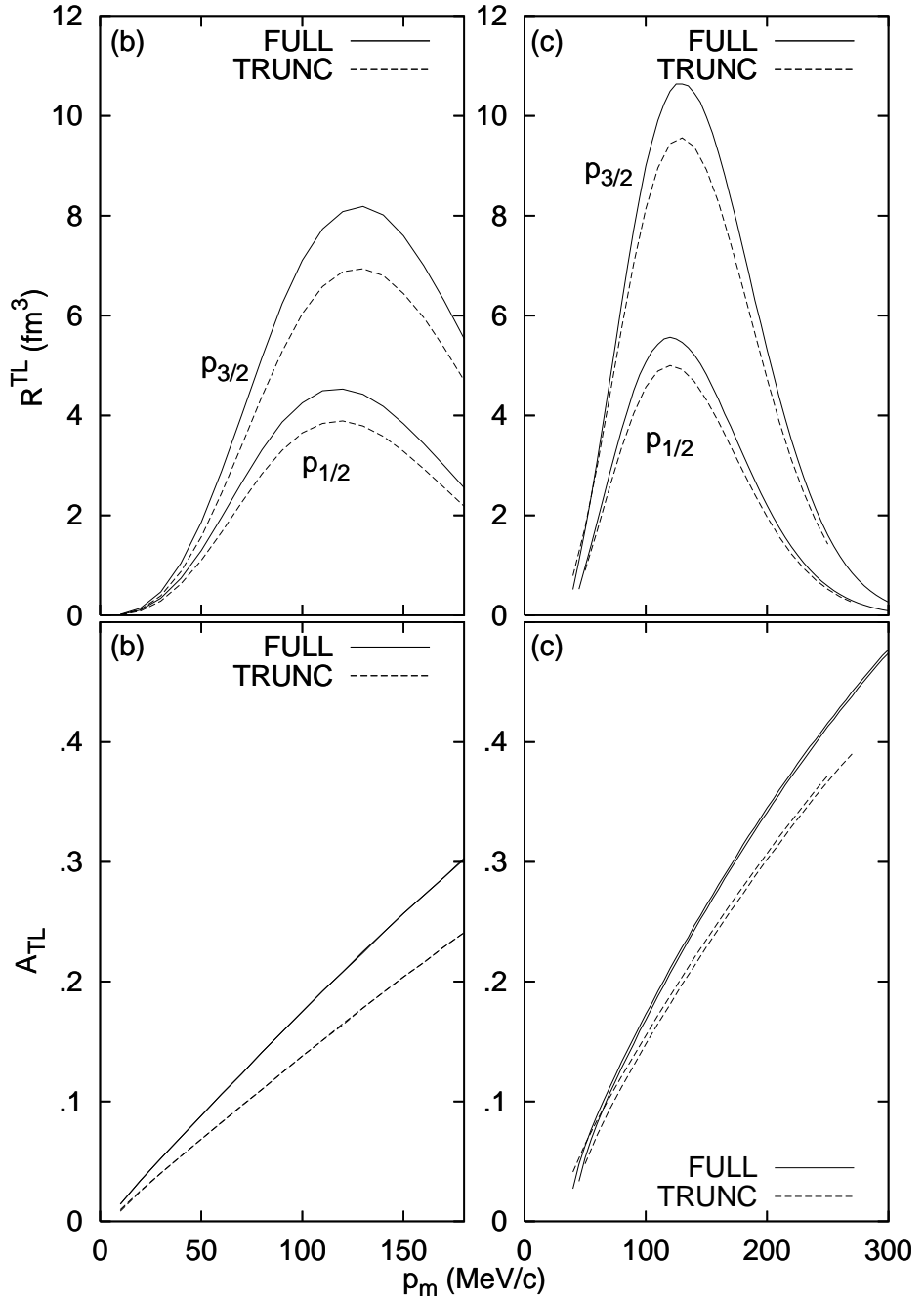


FIG. 9. Same as Figure 8 for R^{TL} and A_{TL} of sets (b) and (c).

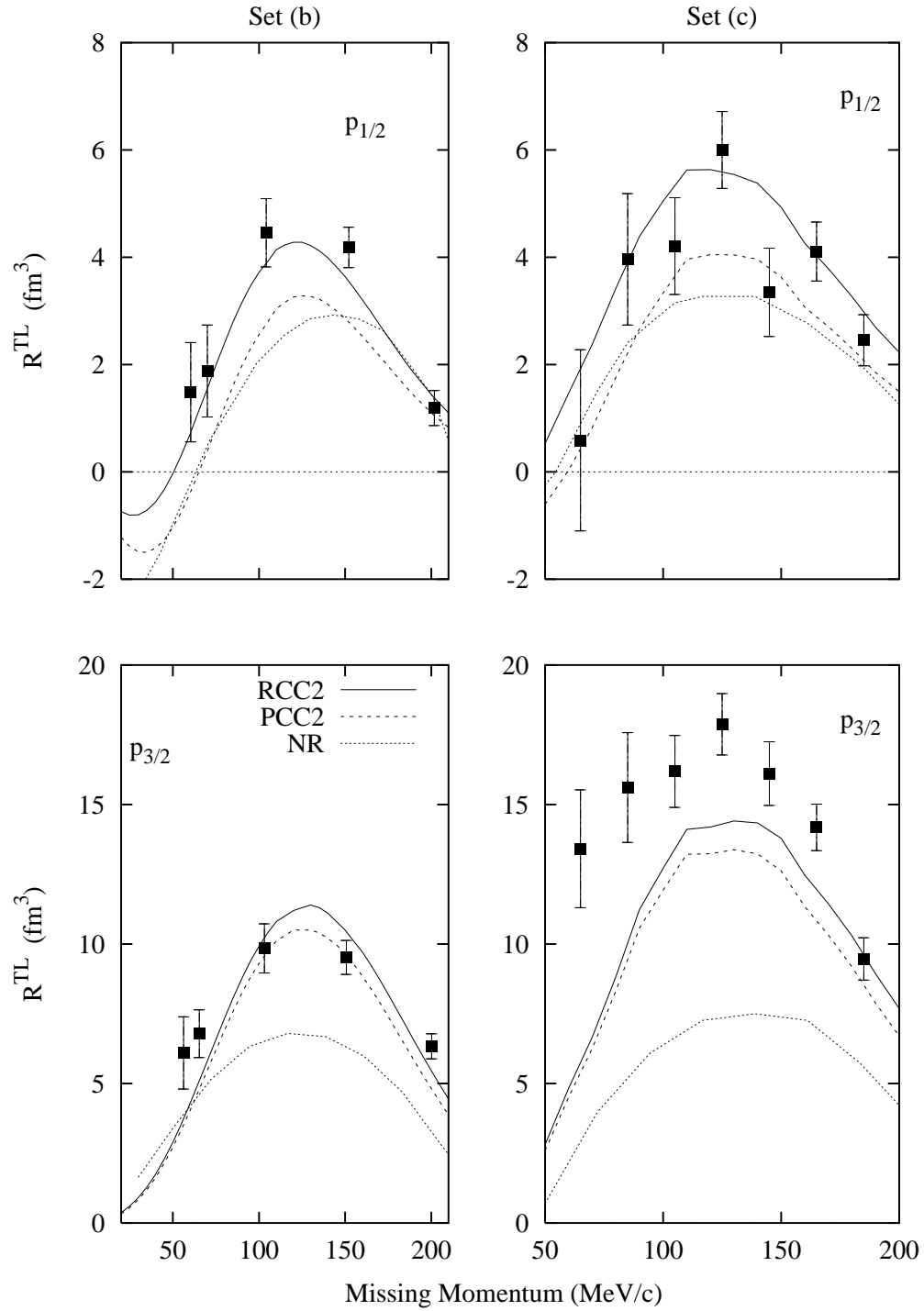


FIG. 10. Relativistic results of this work (solid lines) for R^{TL} compared to projected results (dashed lines) and to nonrelativistic results of ref. [21] (dotted lines). The experimental data are taken from refs. [20] and [21].